Thin–Walled Structures 218 (2026) 113935

Contents lists available at ScienceDirect

Thin-Walled Structures

journal homepage: www.elsevier.com/locate/tws

Full length article

Shape sensing and damage detection of composite pressure vessels using inverse finite element method coupled with physics-based strain pre-extrapolation

Jacopo Bardiani [a,*], Roberto Faure Ragani [a], Lucio Pinello [a], Adnan Kefal [b], Andrea Manes [a], Claudio Sbarufatti [a]

[a] Politecnico di Milano, Department of Mechanical Engineering, Via G. La Masa 1, 20156 Milano, Italy
[b] Faculty of Engineering and Natural Sciences, Sabanci University, Tuzla, Istanbul, 34956, Turkey

ARTICLE INFO

Keywords:
Type IV pressure vessel
Shape sensing
Structural health monitoring
Fiber optic sensors
iFEM
Pre-extrapolation

ABSTRACT

This study presents an advanced strategy for shape sensing and damage detection of composite Type IV pressure vessels using the inverse finite element method (iFEM) coupled with a novel physics-based strain pre-extrapolation approach. The pre-extrapolation methodology, developed based on Kirchhoff plate bending theory, enhances the accuracy of full-field displacement and strain reconstruction by addressing the need for strain input across all structural regions. By incorporating discrete experimental measurements, this framework enables precise residual strain estimation, facilitating damage localization in composite structures. The proposed inverse model is validated through both numerical and experimental investigations, leveraging fiber optic sensor networks strategically placed along axial and circumferential segments of the pressure vessel. Quasi-static compression and low-velocity impact (LVI) tests are conducted to evaluate the model's performance under complex loading conditions. The reconstructed displacement and strain fields demonstrate the exceptional capability of iFEM in accurately capturing structural deformations and detecting damage initiation and progression. Notably, the method effectively identifies damage induced by LVI by analyzing residual strain distributions at critical post-impact time instances. Overall, the results underscore the robustness of the iFEM framework in capturing complex shape deformations and damage patterns that might otherwise remain undetected, highlighting its potential for real-time structural health monitoring of composite pressure vessels.

1. Introduction

The global transition to sustainable energy has spurred extensive research into technologies that reduce greenhouse gas (GHG) emissions and dependence on fossil fuels. Among these, hydrogen stands out as a versatile and renewable energy carrier, producing only water as a byproduct when used in fuel cells or combustion processes [1–3]. As the lightest and most abundant element, hydrogen exists naturally as a bi-atomic, non-toxic, colorless, and odorless gas [4]. Its unique properties make it a cornerstone in the pursuit of decarbonization, particularly in energy-intensive sectors such as transportation, aerospace, and energy storage [5]. Hydrogen offers one of the highest energy densities per unit mass, making it an ideal medium for storing large amounts of energy over extended periods—qualities that surpass the capabilities of batteries. While hydrogen is already widely used in rocket and space applications, its adoption in road, maritime, and air transportation is still limited but actively developing. For instance, the International Maritime Organization has set ambitious targets to reduce GHG emissions from maritime transport by 50 % by 2050 [6]. Similarly, the automotive industry is making significant progress with hydrogen-powered fuel cell electric vehicles, which offer a promising alternative to traditional internal combustion engines [7]. However, achieving these decarbonization goals hinges on the development of robust and efficient hydrogen storage systems capable of withstanding the high pressures required for practical applications [8].

Building on the need for robust and efficient hydrogen storage systems, composite materials have become indispensable in the manufacturing of high-pressure vessels due to their exceptional mechanical properties, including a high strength-to-weight ratio and excellent resistance to impact, fatigue, and corrosion [9,10]. These

* Corresponding author.
E-mail address: jacopo.bardiani@polimi.it (J. Bardiani).

https://doi.org/10.1016/j.tws.2025.113935
Received 6 March 2025; Received in revised form 30 July 2025; Accepted 3 September 2025
Available online 4 September 2025

characteristics make composite pressure vessels the ideal choice for safely storing hydrogen under the high-pressure conditions required for practical applications. Among these, Type IV composite pressure vessels stand out for their advanced design and performance. These vessels feature a polymer liner that acts solely as a hydrogen confinement layer, encased within a load-bearing structure made entirely of composite materials, such as carbon fiber-reinforced epoxy, typically fabricated using filament winding techniques [11]. In more detail, the non-structural liner, commonly made of high-density polyethylene or, less frequently, a thin metallic layer, ensures hydrogen containment, while the external composite layers bear the mechanical load. Additionally, a metallic boss integrated into the dome facilitates the installation of sensors and valves, ensuring operational functionality [12]. Although Type IV vessels are more expensive to produce compared to lower-tier designs [13], their superior performance justifies their cost. These vessels can safely store hydrogen at pressures of up to 70 MPa, enabling electric vehicles to achieve driving ranges of 300 to 500 miles with 4–10 kg of hydrogen [14]. Their lightweight construction, combined with compliance with stringent safety standards, makes them critical for advancing hydrogen adoption across diverse sectors, including automotive, aerospace, and maritime industries [15,16].

While Type IV pressure vessels offer numerous advantages for hydrogen storage, ensuring their structural integrity and long-term reliability under high-pressure and dynamic loading conditions remains a critical challenge. These vessels operate in extreme environments where even minor defects or damage can lead to catastrophic failure. The demand for lightweight designs, essential for applications like fuel cell electric vehicles and aerospace systems, further complicates this issue, as reducing vessel weight often introduces manufacturing complexities and narrows safety margins. Additionally, hydrogen, despite its promise as a clean energy carrier, poses significant safety challenges due to its high pressure, volatility, and flammability, particularly in the event of storage tank damage. Hydrogen embrittlement and leakage risks exacerbate these concerns, necessitating advanced materials and stringent testing protocols to ensure safe storage and operation [17]. The challenges intensify in applications such as aerospace and marine systems, where pressure vessels are exposed to a variety of static and dynamic loading conditions, including impacts and environmental stresses. These factors heighten design complexity and safety demands, making continuous structural health monitoring essential.

Advanced structural health monitoring (SHM) systems have emerged as a key solution, enabling the accurate detection and localization of damage, real-time deformation monitoring, and comprehensive insights into vessel performance. SHM employs onboard sensors to evaluate the health status of structures, facilitating the early identification of potential issues, which bolsters safety and optimizes maintenance efforts [18,19]. By integrating SHM technologies into the design and operation of Type IV pressure vessels, maintenance costs can be reduced while structural safety is significantly enhanced. This proactive approach to monitoring ensures that potential damage is identified and addressed before it escalates, thereby supporting the reliable adoption of hydrogen storage systems across automotive, aerospace, and marine industries. In general, the implementation of SHM tasks involves a range of methods, primarily classified as data-driven and model-based techniques. Data-driven approaches leverage machine learning or pattern recognition algorithms to analyze structural behavior based on collected datasets [20]. In contrast, model-based techniques usually necessitate the creation of a detailed model that effectively simulates the structure's response in both healthy and compromised states for a comprehensive assessment [21].

Among the various model-based methods in the literature [22], the inverse finite element method (iFEM) [23,24] stands out for its ability to determine displacement distributions within a structure using discrete strain measurements. The original iFEM formulation [23,24] minimizes an error functional, defined as the least-squares difference between measured and numerically formulated strains. It requires only experimental measurements, a mesh discretization of the structure, and the definition of structural constraints, with no dependence on applied external loads and material properties. Various inverse finite elements have been developed to support shape sensing and structural health monitoring applications. Notable shell elements, such as iMIN3 (three-node flat shell element based on Mindlin theory, [25]), iQS4 (inverse Quadrilateral Shell element with 4 nodes, [26]), and iCS8 (inverse Curved Shell element with 8 nodes, [27]), employ first-order shear deformation theory with C0-continuous interpolation functions. Among these, iQS4 element has garnered significant attention due to its effectiveness in modeling large-scale systems with low-cost sensor networks and its ability to provide highly accurate displacement predictions. The iQS4 element has been widely applied to ships such as container ships [28,29], bulk carriers [30], chemical tankers [31], offshore platforms [32], and aerospace structures [33–35], and even beam-like structures [36]. Beyond displacement reconstruction, the iQS4/iFEM approach has proven to be robust in detecting damage in both isotropic and orthotropic materials, as well as in monolithic and stiffened structures [37–39]. The method has also been employed for identifying pitting corrosion [40], reconstructing complex loads [41], and modal shape identification [42], demonstrating its versatility and robustness. Apart from shell elements, inverse-beam elements have similarly been developed for real-time deformation monitoring in thin and thick beam structures [43–45]. More recently, the iFEM framework has also been extended by coupling it with Generalised Beam Theory (GBT) to enhance shape sensing and damage detection capabilities in thin-walled cylindrical and conical shell structures, further broadening its applicability to several pressure vessel configurations [46,47]. These elements have demonstrated high accuracy and efficiency in experimental and numerical investigations, particularly when integrated with fiber Bragg grating sensors for dynamic displacement predictions [48–50].

The versatility of iFEM is further evident in its application to multilayered and sandwich composite structures, where it has been employed for displacement and stress monitoring under varying load conditions. Recent developments have incorporated refined theories to enable accurate reconstruction of zigzag deformations across the thickness of sandwich plates [51,52] and beams [53]. This method has been validated through numerical and experimental studies for moderately thick sandwich panels, particularly in aerospace applications [54]. Experimental implementations have demonstrated its practicality for real-time shape and strain sensing in composite panels, including those subjected to impact damage or complex boundary conditions [55]. Moreover, the iFEM methodology has been applied to complex scenarios such as the detection of delamination damage in composite structures [56,57] and real-time crack propagation monitoring in fiber-reinforced composites [58,59]. These advancements highlight the adaptability and robustness of iFEM for SHM in modern engineering applications. The iFEM method, however, faces limitations in practical applications due to the uneven placement of sensors across the structure. Hardware and accessibility constraints often restrict sensor deployment, reducing the accuracy of displacement reconstruction. To address this, the isogeometric iFEM approach [60] has been developed, utilizing non-uniform rational B-splines to enhance the precision and smoothness of deformation reconstruction, even with limited sensors. Additionally, strain pre-extrapolation techniques [61–66] are frequently employed to estimate strain data in regions without sensors, significantly improving accuracy of low-cost shape sensing applications. It is worth noting that all previously reported pre-extrapolation methods rely primarily on curve-fitting or crack-based formulations and do not incorporate the actual governing equations of plate or shell mechanics, thus limiting their ability to produce physically consistent strain fields in structurally complex and curved composite systems.

Despite the extensive advancements in the iFEM methodology, the literature reveals a significant gap in its application to Type IV composite pressure vessels, which are critical for hydrogen storage in several

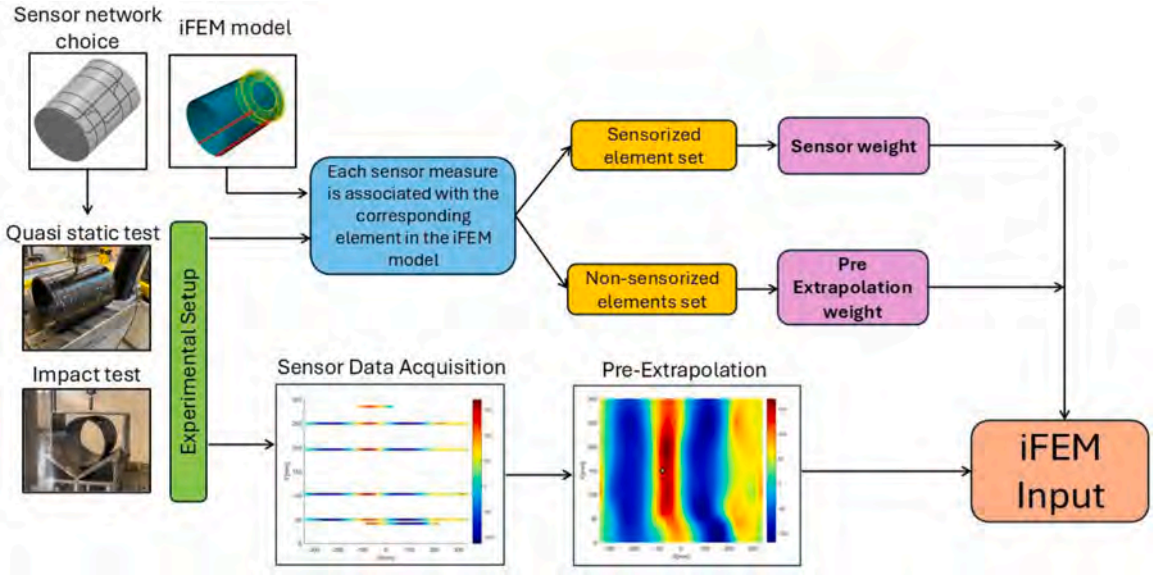

Fig. 1. Workflow chart of the simulation process performed in the presented study.

real-world applications. This study addresses that gap by introducing a combined numerical-experimental methodology for shape sensing and damage detection in Type IV composite pressure vessels. The key innovations of the proposed approach can be summarized as follows:

(1) First known application of iFEM to Type IV pressure vessels under complex loading:
This work presents the first application of iFEM to Type IV composite vessels subjected to quasi-static loads and low-velocity impacts—conditions highly relevant to operational safety but not yet explored in this context.
(2) Coupling with physics-based strain pre-extrapolation:
The iFEM formulation is enhanced by integrating a strain pre-extrapolation procedure based on plate theory, enforcing biharmonic constraints. This physics-informed approach enables accurate strain estimation even in regions with sparse sensor data, significantly improving the quality of the inverse solution.
(3) Post-impact damage detection based on residual strain reconstruction:
The iFEM results are used not only for shape sensing but also to detect impact-induced damage by analyzing residual strains after the event. As shown in the final part of the paper, the method effectively identifies localized permanent deformations, demonstrating its reliability in experimental settings—an aspect rarely addressed successfully in the existing literature.

The paper is structured as follows. Section 2 presents the theoretical framework of the iFEM formulation and its coupling with the physics-based strain pre-extrapolation strategy. Section 3 outlines the numerical and experimental studies, detailing the experimental sensor network, the acquisition of strain measurements, and their integration into the iFEM framework. Also, it discusses the results obtained, including the reconstruction of full-field displacement and strain for various scenarios investigated. Section 4 concludes the paper, summarizing key findings and their implications for future research and applications.

2. The iFEM methodology with physics-based strain pre-extrapolation

Fig. 1 presents the flowchart of the strategy implemented in this work, which is further described in this section. A summary of the iFEM approach to displacement and strain field reconstruction is provided here, while a detailed formulation is available in Refs. [26–28,64] for the interested reader.

Assume a shell structure is discretized into inverse elements, specifically the iQS4 is adopted in this study [26]. The displacement field is calculated from input strain measurements by minimizing the least-square functional of Eq. (1), which is defined as the error between the input strain field measured by sensors $(\cdot^{\varepsilon})$ and its numerical formulation $(\cdot(\boldsymbol{u}))$, which is a function of the unknown nodal displacements $\boldsymbol{u}$. Both the input and numerical strain fields are separated into three main components: the membrane $\boldsymbol{e}$, the bending $\boldsymbol{k}$, and the

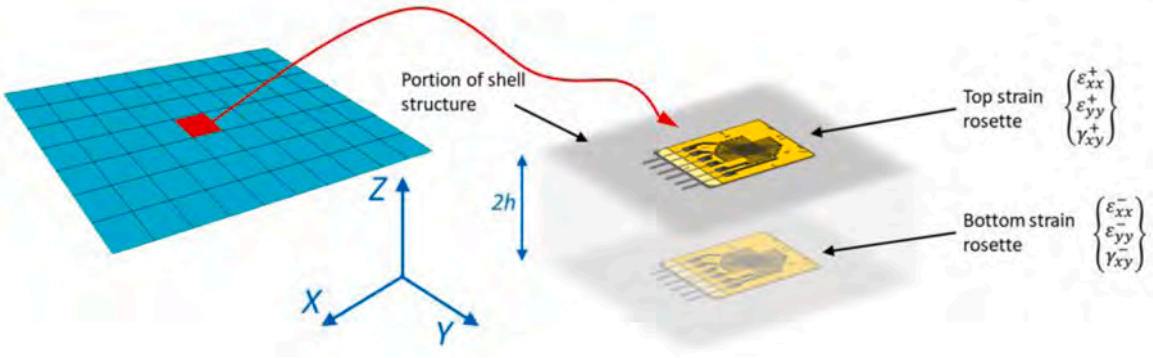

Fig. 2. Discrete sensor placement on both the top and bottom surfaces of the shell structure (adapted from Ref. [57]).

transverse shear g strain contributions. Thus, the formulation of the i th inverse element can be defined as:

$$\Phi_i(\boldsymbol{u}^i) = \| \boldsymbol{e}(\boldsymbol{u}^i) - \boldsymbol{e}_i^{\varepsilon} \|^2_{\boldsymbol{W}_m^i} + \| \boldsymbol{k}(\boldsymbol{u}^i) - \boldsymbol{k}_i^{\varepsilon} \|^2_{\boldsymbol{W}_b^i} + \| \boldsymbol{g}(\boldsymbol{u}^i) - \boldsymbol{g}_i^{\varepsilon} \|^2_{\boldsymbol{W}_s^i} \quad (1)$$

Where $\| \cdot \|^2_{\boldsymbol{W}}$ is the squared weighted Euclidean norm with the weight matrix $\boldsymbol{W}$. Specifically, $\boldsymbol{W}_m^i$, $\boldsymbol{W}_b^i$, and $\boldsymbol{W}_s^i$ are diagonal matrices of weights for the membrane, bending, and transverse shear strain contributions, respectively. These coefficients ensure coherence between the numerical and experimental strain measurements, especially in the case of sparse sensor networks. Generally, a unitary reference value is assigned to elements where the input strain field component is measured by physical sensors ($\boldsymbol{e}_i^{\varepsilon}$, $\boldsymbol{k}_i^{\varepsilon}$ and $\boldsymbol{g}_i^{\varepsilon}$), while in other cases (missing in-situ strain component), the coefficients are reduced to small values (e.g., 10^{-4}). Note that each matrix $\boldsymbol{W}$ contains three weights on the main diagonal, which correspond to the strain components along the x-axis, the y-axis, and the in-plane shear with respect to the element's local reference system (Fig. 2).

In the broadest scenario, the input strain formulation is derived from strain measurements taken on the structure. Sensors are typically placed on the external surfaces of the component for easier installation and maintenance, although applications with embedded sensors are also feasible.

For example, consider a couple of strain gauge rosettes applied on the two external sides of the shell as shown in Fig. 2. The membrane and the bending strain components associated with the j-th sensors' location within the i th inverse element can be defined as following:

$$\boldsymbol{e}_{ij}^{\varepsilon} = \frac{1}{2} \begin{Bmatrix} \varepsilon_{xx}^{+} + \varepsilon_{xx}^{-} \\ \varepsilon_{yy}^{+} + \varepsilon_{yy}^{-} \\ \gamma_{xy}^{+} + \gamma_{xy}^{-} \end{Bmatrix}_j \quad \boldsymbol{k}_{ij}^{\varepsilon} = \frac{1}{2h} \begin{Bmatrix} \varepsilon_{xx}^{+} - \varepsilon_{xx}^{-} \\ \varepsilon_{yy}^{+} - \varepsilon_{yy}^{-} \\ \gamma_{xy}^{+} - \gamma_{xy}^{-} \end{Bmatrix}_j \quad (2)$$

Where $2h$ is the shell thickness at the sensors' location.

The strain component g, on the other hand, cannot be directly computed from the measured surface strain components. However, since its contribution can be neglected in most engineering applications, the g formulation is neglected hereon.

The numerical strain components formulation is based on the element's shape functions, thus, it is computed through Eq. (3), where $\boldsymbol{B}^m$, $\boldsymbol{B}^b$, and $\boldsymbol{B}^s$ are matrices containing the derivative of the shape functions [26–28].

$$\begin{aligned} \boldsymbol{e}(\boldsymbol{u}^i) &= \boldsymbol{B}^m \boldsymbol{u}^i \\ \boldsymbol{k}(\boldsymbol{u}^i) &= \boldsymbol{B}^b \boldsymbol{u}^i \\ \boldsymbol{g}(\boldsymbol{u}^i) &= \boldsymbol{B}^s \boldsymbol{u}^i \end{aligned} \quad (3)$$

After some passages applied to Eqs. (2) and (3) inside Eq. (1), by employing a conventional assembly procedure that accounts for the contribution of each inverse element and aims to minimize the overall least-squared functional, the problem can be formulated as follows:

$$\boldsymbol{K}\boldsymbol{U} = \boldsymbol{F} \quad (4)$$

Where $\boldsymbol{K}$ is a matrix resembling the stiffness linking the global displacement field $\boldsymbol{U}$ with the vector $\boldsymbol{F}$ containing the input strain field contribution.

Nonetheless, the matrix $\boldsymbol{K}$ is singular and, if left unconstrained, it will result in a rigid motion of the structure. Therefore, after establishing appropriate boundary conditions, the free (unconstrained) nodal displacement can be determined. Subsequently, once the displacement field has been calculated, the numerical strain field $\boldsymbol{\epsilon}^{iFEM}$ can be computed using Eq. (3), similarly to any direct FEM approach. What we have seen is that a model $\boldsymbol{M}_{iFEM}$ is available for real-time numerical prediction of the strain field $\boldsymbol{\epsilon}_{iFEM}$, as a function of vector of strain measurements $\boldsymbol{\epsilon}_{in}$, without requiring any a-priori knowledge of loads or material properties since only strain-displacement relationships are involved in the calculations.

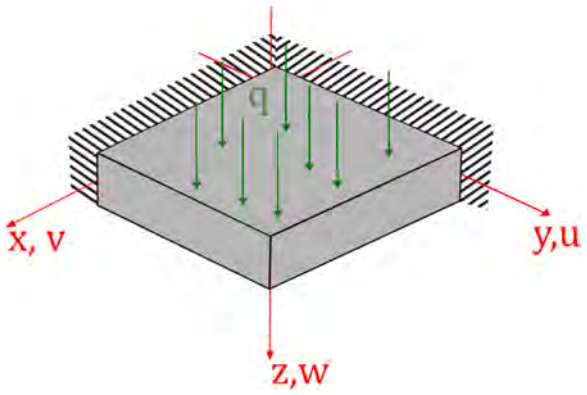

Fig. 3. Schematic representation of a plate under a distributed load.

For precise reconstruction of the displacement field, it is necessary to have the input strain field available for all elements of the structure. However, this is generally impractical in real-world applications, due to costs and impracticability issues. To address this limitation, strains can be extrapolated in areas where physical sensors are unavailable. This can be achieved through methods such as polynomial fitting or Smoothing Element Analysis (SEA) [61,64,65], utilizing either data-driven or physics-based approaches. Data-driven methods extrapolate strains solely based on the acquired strain field, resulting in a more continuous and smooth output across the entire domain. Conversely, physics-based strain extrapolation combines the acquired strain data with knowledge of geometrical discontinuities and their analytical formulations to provide a more accurate strain field, especially in the presence of discontinuities. By incorporating physical principles into the extrapolation process, the estimated measurements closely resemble those that would be obtained from an actual sensor at the same locations, thus improving the robustness of the reconstruction. For this reason, an important aspect is the calibration of the coefficient within the weight matrix $\boldsymbol{W}$ when using pre-extrapolated values.

In this paper, a physics-based strain extrapolation strategy is implemented based on the fundamentals of the Kirchhoff-Love theory of bending plates, as it leverages the underlying mechanical behavior of the structure to enhance the accuracy of the inferred strain field. This approach is fully consistent with the assumptions typically adopted in inverse FEM procedures. Although the iQS4 element is based on Mindlin-Reissner theory and accounts for shear deformation, transverse shear strains are commonly neglected in the inverse formulation, as their contribution is generally minor compared to in-plane strains and curvatures. In our case, the radius-to-thickness ratio of the pressure vessel ($\approx$ 12.15 in the present case) confirms its thin-shell behavior, justifying this simplification. Therefore, using Kirchhoff-Love theory during the pre-extrapolation step—as a physical constraint to interpolate strain fields in unsensorized regions—is not only appropriate but also consistent with standard practices in iFEM literature.

The Kirchhoff plate theory governs the behavior of thin plates under bending and provides a framework for modeling their deflection, $w(x, y)$, due to applied loads. The theory is based on equilibrium conditions, compatibility relations, and the constitutive equations of elastic materials [67].

According to the Kirchhoff theory [67,68], the equilibrium condition for a thin plate under transverse distributed load $q(x, y)$ (Fig. 3) is given by:

$$\frac{\partial^2 M_x}{\partial x^2} + \frac{\partial^2 M_y}{\partial y^2} + \frac{2\partial^2 M_{xy}}{\partial x \partial y} + q(x,y) = 0 \quad (5)$$

Where M_x, M_y and M_{xy} are the bending moments and torsional moment per unit width, respectively. These moments are related to the plate's curvature by the constitutive relations:

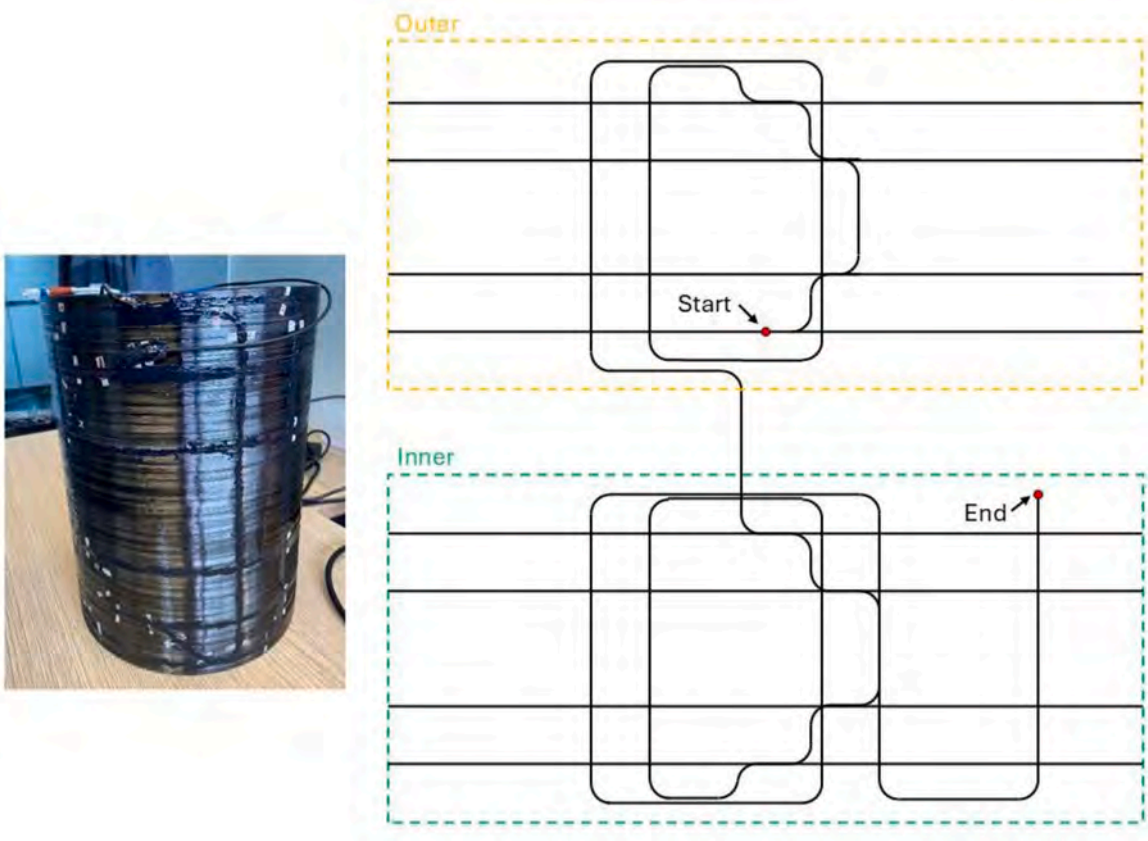

Fig. 4. Schematic view of the sensor network arranged in the unwrapped configuration.

$$M_x = -D\frac{\partial^2 w}{\partial x^2}$$
$$M_y = -D\frac{\partial^2 w}{\partial y^2} \quad (6)$$
$$M_{xy} = -D\frac{\partial^2 w}{\partial x \partial y}$$

In which D is the flexural rigidity of the plate, defined as:

$$D = \frac{E(2h)^3}{12\cdot(1-\nu^2)} \quad (7)$$

Where E is the Young's modulus, ν is the Poisson's ratio, and $2h$ is the plate thickness (in accordance with Fig. 2).

Substituting the expressions for the moments into the equilibrium equation leads to the governing equation for the plate's deflection:

$$-D\left[\frac{\partial^4 w}{\partial x^4} + \frac{\partial^4 w}{\partial y^4} + \frac{2\partial^4 w}{\partial x^2 \partial y^2}\right] + q(x,y) = 0 \quad (8)$$

Where the operator inside the brackets is the biharmonic operator ∇^4. Thus, the equation can be rewritten as:

$$\nabla^4 w = \frac{q(x,y)}{D} \quad (9)$$

In the absence of transverse distributed loads ($q(x,\ y) = 0$), the governing equation simplifies to:

$$\nabla^4 w = 0 \quad (10)$$

This condition represents the behavior of a plate structure with no distributed loads. In the present case, the loads acting on the structure are almost entirely point-like, making this equation nearly satisfied within the structure. It is therefore suitable for providing additional information about the strain field distribution prior to the iFEM reconstruction.

For carrying out a scatter strain extrapolation maintaining the null biharmonic constraint, according to Eq. (10), the Matlab v4 function was exploited. This method employs Green's functions to generate smooth surfaces with minimal curvature. It leverages the biharmonic equation, which ensures a surface with minimal energy. The core idea is based on finding a function $G(r)$ that satisfies the biharmonic equation:

$$\nabla^4 G(r) = \delta(r) \quad (11)$$

Where the term $\delta(r)$ is the Dirac delta function, r is the position vector in the 2D domain (unwrapped cylinder in this specific case). In this context, r represents the Euclidean distance between the evaluation point and the location of the source (known strain points) and is used in the formulation of the Green's function solution. The solution in two dimensions for the biharmonic equation in Eq. (11) is given by the following [69]:

$$G(r) = r^2\ (log(r)\ -\ 1) \quad (12)$$

Among the different steps involved in this procedure, the first one is the calculation of a distance matrix containing the Euclidean distances between known strain points and unknown ones. Using these distances, a Green's function matrix is built, where each element represents the influence of one data point on another. Then, to determine the interpolated surface, a system of linear equations is solved using the Green's function matrix. For any query point, the interpolated value is computed as a weighted sum of the Green's function values between the query point and all known data points. This ensures smooth transitions and continuity across the entire surface respecting the null biharmonic constraint.

In the present research, the selection of sensor positions was the outcome of a preliminary multidisciplinary design process aimed at

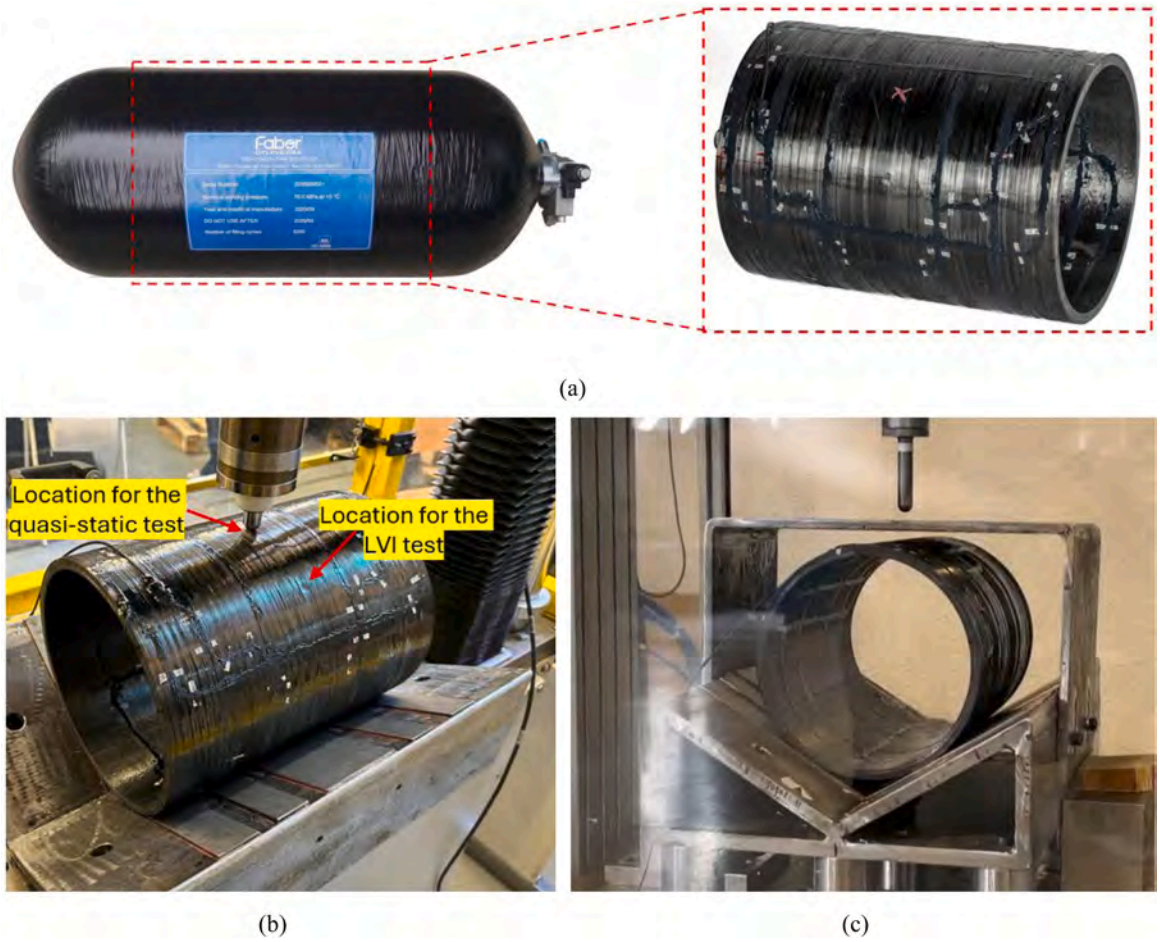

Fig. 5. Prototype of the pressure vessel under investigation: (a) cylindrical specimen 10 m optical fiber strain sensor, (b) experimental quasi-static test and (c) experimental low velocity impact test.

achieving an effective balance between monitoring accuracy, physical feasibility, and implementation constraints. Rather than relying solely on theoretical optimization, the sensor layout was developed through collaboration between the research team, the pressure vessel manufacturer, and optical sensing experts. This process integrated prior numerical insights, such as FE-based estimations of strain distributions under representative loading scenarios, with engineering experience and technological considerations related to fiber optic systems.

Several practical and physical criteria guided the design, including the need to:

- Avoid sharp directional changes to prevent signal loss or fiber damage.
- Minimize undesired load transfer through the fiber, which could interfere with measurement quality.
- Maximize straight segments to ensure clear acquisition directions and facilitate data interpretation.
- Provide strain data in both axial and circumferential directions for robust biaxial field reconstruction.

Additionally, constraints related to manufacturing and vessel geometry—such as the curvature of the surface, internal accessibility, and limitations of manual sensor placement—were carefully considered. The resulting layout, while not the product of a formal optimization routine, represents a practically sound and technically effective solution, as confirmed by the high quality of the experimental strain measurements and the reliability of the iFEM reconstructions presented in later sections.

Fig. 4 illustrates the adopted sensor network, designed to provide sufficient spatial resolution while ensuring mechanical compatibility and measurement robustness.

3. Numerical and experimental application

This section describes the benchmark case under investigation, focusing on experimental tests, the sensor network and the inverse FE model with physics-based pre-extrapolation.

3.1. The specimen and experimental tests

The dimensions of the sample (a simple opened cylinder representative of the lateral side of the vessel) were 226 mm in diameter, 300 mm in length and a total thickness of approximately 9.3 mm (see Fig. 5(a)). The material for the prototype sample analyzed in this study was produced by Faber Industrie SpA, through the filament winding process using carbon fiber-reinforced plastic, specifically Toray™ T700S, combined with LY 3585 bisphenol-A epoxy resin from Huntsman™, cured with Aradur™ 3486. The cylindrical specimen was obtained by removing the domes of a vessel through mechanical cutting and subsequent removal of the plastic liner inside.

The fiber layup is the one used in commercial vessels, composed by external hoop layers (with fibers aligned perpendicular to the vessel's axis) and internal layers predominantly helical (notation used for layers in which the fibers are laid at an angle different from 90°). The specific details of the latter layup are not disclosed in this context due to their proprietary and confidential nature as an industrial secret.

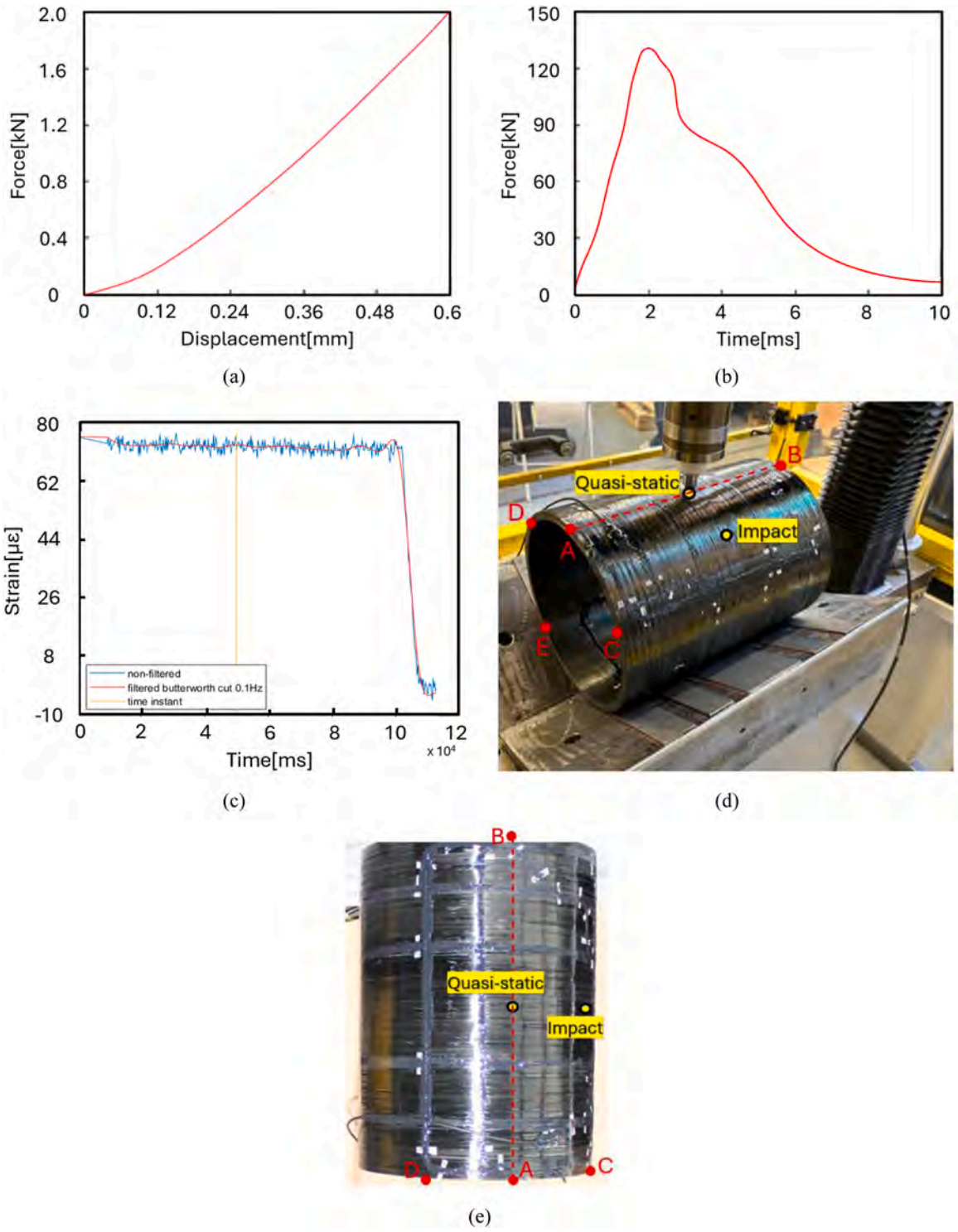

Fig. 6. (a) Force [kN] vs. displacement [mm] curve for the loading phase of the quasi-static compression test. (b) Force [kN] vs. time [ms] curve (filtered) for the impact test. (c) example of the filtering process of the experimental measurements taken from sensor n°200 (see Fig. 8(a)) through Butterworth filter (quasi-static test). (d) indication of some representative points of the cylinder for better comprehension of the results. (e) indication of the same points in (d) but in a different view of the sample.

Several experimental tests were specifically designed to evaluate the effects of several loading conditions on the mechanical behavior of the pressure vessel. They involved a sequence of quasi-static and dynamic low velocity impact events, aimed at determining how these events alter the response of the composite prototype. To maximize the acquired data per tested specimen, an optical fiber strain sensor was applied to the specimen and Section 3.2 deals with the sensorization strategy exploited.

Regarding the quasi-static compression test, an MTS Alliance RF/150 testing machine was used. The machine head was positioned halfway along the length of the cylinder, in a sensor-free zone (see "X" mark in Fig. 5(a) and (b)), using a hemispherical penetrator with a diameter equal to 25 mm. The quasi-static compression test was characterized by three phases: a loading phase where the load on the specimen increased

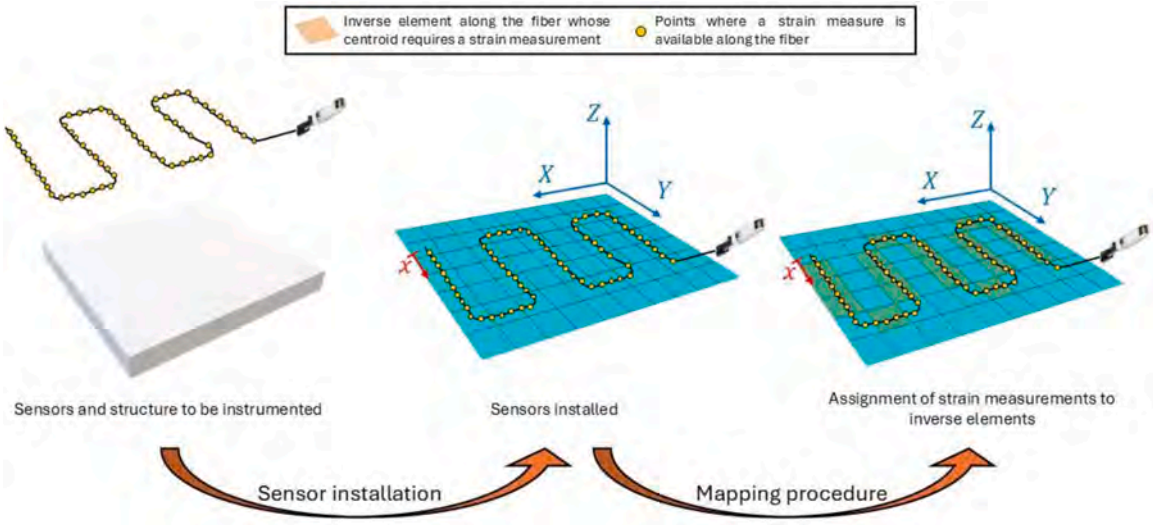

Fig. 7. Schematic illustration of the mapping process used to associate fiber-optic sensor measurements with specific physical locations on the specimen's surface for a representative plate. Yellow dots represent all available measurements along the fiber, while highlighted elements indicate those whose centroids require a strain input. The yellow points closest to each centroid were selected as input measurements.

up to a value of 2 kN (Fig. 6(a)), a constant loading phase (designed to keep the vessel within the elastic range), and finally an unloading phase. This test was carried out in accordance with what was done in [70], in which quasi-static compression of thick CFRP rings produced by filament winding was investigated.

Regarding the dynamic test, an LVI test was performed using a drop-tower apparatus according to the ASTM D7136 standard [71]. The sample was impacted by a hemispherical impactor (16 mm diameter) halfway along the length of the cylinder, also in this case in a sensor-free zone, but in a different position with respect to the quasi-static test (Fig. 5(b) and (c)). The velocity of the impactor at the onset of contact with the target (approximately 4.2 m/s) was measured using an optical sensor and a load cell was used to record the contact force between the impactor and cylinder during the impact (Fig. 6(b)). The LVI test was characterized by an impact energy equal to 105 J. A C-shaped steel cover was used to protect the machine from the impactor's sliding. No high-speed camera was used, as the loading and displacement curves were deemed sufficient for the purposes of this study. After the tests, the impactor displacement, and loading force overtime were recorded. To validate the experimental data, at least two tests were conducted under the same conditions but for different samples, yielding consistent results and confirming the reliability of the experimental investigations.

For the present research, strain patterns corresponding to the middle time instant of the constant loading phase of the quasi-static compression test were extracted, along with five patterns corresponding to the impact test (0.05, 0.5, 1, 1.5 and 2 ms of Fig. 6(b)) and one sufficiently after the impact, the latter for residual strain evaluation.

In both experimental tests considered, a V-shaped steel support was specifically designed and produced to stabilize the specimen during the test (Fig. 5(b)). This support configuration not only ensures a stable test setup but also minimizes the likelihood of damage at the support interface, as the load is more evenly distributed compared to the impact area. To prevent any contact between the sensor and the steel support, aluminum plates were affixed to the support surface, creating sufficient space to accommodate the fiber circumferential loops. The damage induced by the impact test, although minimal and limited in extent, is shown in Fig. 5(b).

3.2. The sensor network and its installation

The sensor used was the HD6S10LC300P from Luna Innovations [70], a high-definition optical fiber strain sensor with an overall length of 10 m (5 m are glued on the outer surface and the rest on the inner surface). The high-definition optical fiber sensor provided approximately 1000 measurement points along the sensing path, evenly distributed between the inner and outer surfaces of the structure. This sensor needs to be connected to a control unit to perform measurements.

The operating principle of this sensor involves sending an input light signal through the optical fiber using an interrogator. When the light encounters internal defects in the fiber, a portion of it is reflected to the interrogator. Variations in the light's travel time allow the sensor to operate as an ultra-high-resolution axial strain sensor. The output is typically averaged over predefined segment lengths, with overlapping segments ensuring continuous measurement. The opposite end of the fiber is equipped with a metallic termination to reflect any residual light.

The experimental sensor network configuration used as input for the iFEM was essential for the purpose of the research. A mix of axial and circumferential segments was utilized to capture biaxial strain data along both the axial and circumferential directions of the outer layer, facilitating correlation with the FEM output. The proposed sensor path is partially illustrated in Fig. 5(a)-(c) and totally unrolled in Fig. 8 and Fig. 9, where the correspondence with some points of the pressure vessel (Fig. 6(d) and (e)) is shown for greater clarity. The route begins on the external surface of the cylinder and then transitions to the internal one, following similar paths but not exactly overlapping. This similarity in the sensor trajectories was a design choice made by the authors to facilitate post-processing and interpretation. However, a perfect overlap between internal and external paths was not feasible due to practical challenges related to the manual installation of the fiber, especially on the inner surface of the curved pressure vessel, where visibility and accessibility are limited. It is important to note that this is not a requirement of the iFEM methodology, which can accommodate completely independent sensing paths on different surfaces.

The guiding principles for the sensor network design included the following aspects: avoiding sharp directional changes to prevent signal loss or potential fiber damage, preventing load transfer through the fiber which could compromise sensor function and finally maximizing straight segments to ensure well-defined acquisition directions and effective averaging.

Prior to sensor installation, the surface of the vessel was meticulously prepared to ensure optimal sensor adherence, thus signal accuracy. This preparation involved an initial sanding of the surface followed by thorough cleaning with acetone. The fiber sensor was then manually positioned on the specimen's surface and temporarily secured using

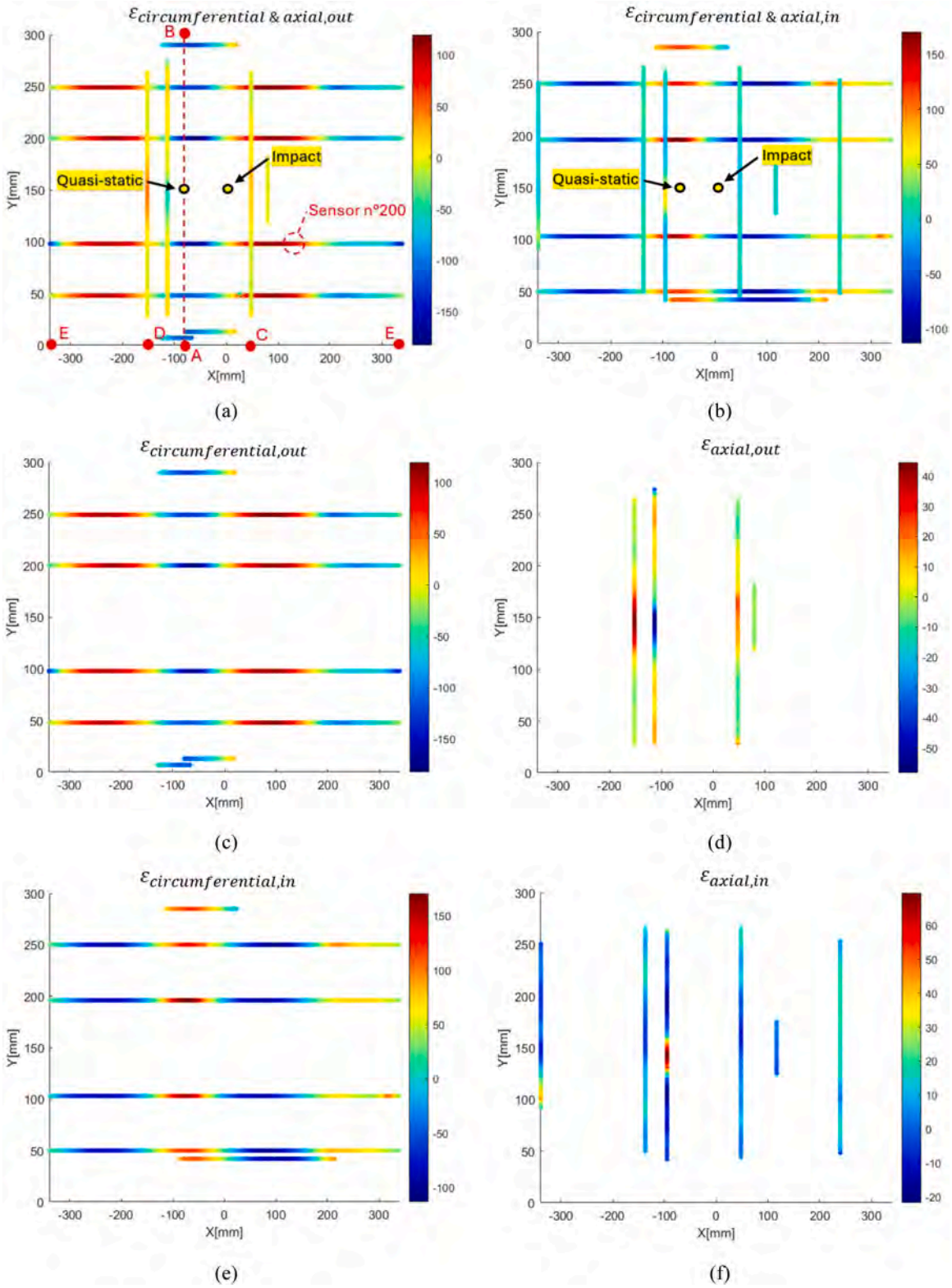

Fig. 8. Unrolled strain gauges measurements extracted to the experimental sensor network in the case of quasi-static test (unit of measurement: [$\mu\varepsilon$]): (a) $\varepsilon_{circumferential\ \&\ axial}$ (external side), (b) $\varepsilon_{circumferential\ \&\ axial}$ (internal side), (c) $\varepsilon_{circumferential}$ (external), (d) ε_{axial} (external), (e) $\varepsilon_{circumferential}$ (internal) and (f) ε_{axial} (internal). The points indicated in (a) are valid for all figures.

paper tape. Once the entire sensor was correctly placed, the mapping process of the relevant points was undertaken. This step, schematically illustrated in Fig. 7, was crucial for accurately converting the distance from the fiber connector, as read by the control unit, to specific physical points on the specimen's surface. As shown in the representative example of Fig. 7, the available measurement locations along the fiber (yellow dots) were then associated with the centroids of the inverse elements requiring a strain input. For each of these elements, the nearest measurement point was selected and used as input for the inverse reconstruction. Following the mapping process, 3M® DP490 epoxy

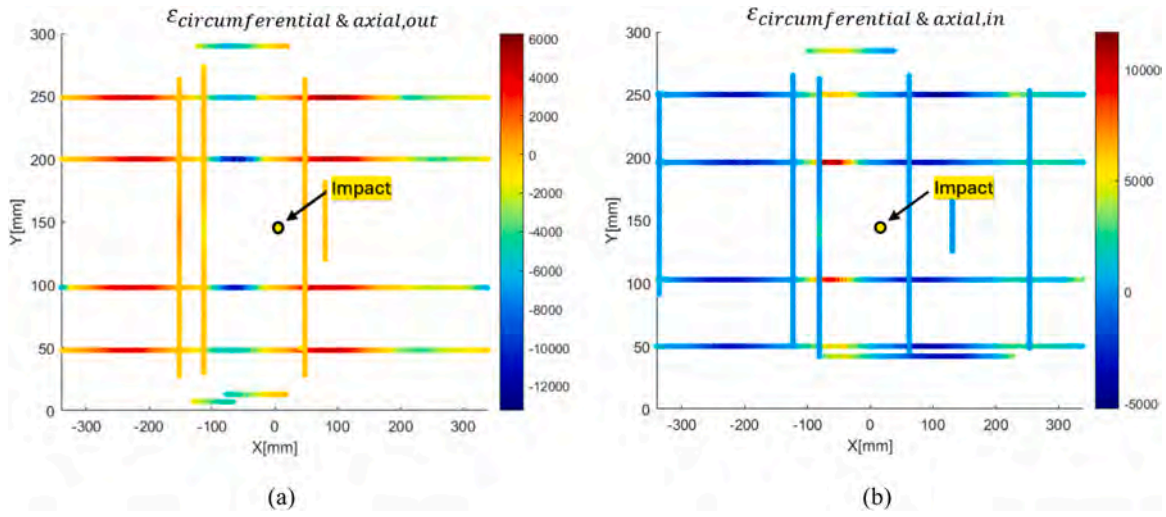

Fig. 9. Unrolled strain gauges measurements extracted to the experimental sensor network when it comes to the impact test (instant of maximum displacement of the impactor, unit of measurement: [$\mu\varepsilon$]): (a) $\varepsilon_{circumferential\ \&\ axial}$ (external side) and (b) $\varepsilon_{circumferential\ \&\ axial}$ (internal side).

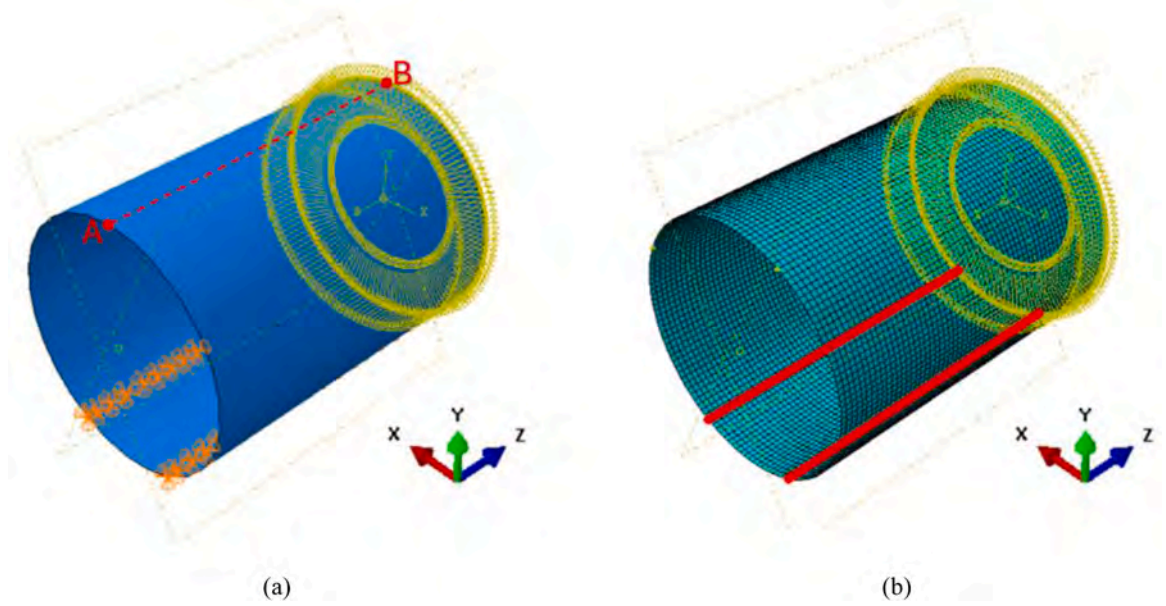

Fig. 10. Inverse FE model in ABAQUS CAE: (a) assembly 3D view with BCs and (b) iQS4 mesh.

structural adhesive was applied to achieve a permanent and reliable attachment to the cylinder's surface. This adhesive step was crucial as the glue should ensure a consistent transfer of strain from the specimen's surface to the sensor, thus it needs to be carefully applied to avoid excessive thickness which could potentially introduce measurement artifacts. To protect the sensor at transition points where the fiber is disconnected from the specimen, particularly at the beginning of fiber route and at the transition from the external side to the internal one, a rubber heat shrink tube was employed.

The different locations for the impacted points in quasi-static and impact tests (Fig. 5(b)) were chosen based on preliminary studies, to preserve the integrity of the fiber and to prove that this sensor network can capture the behavior of the entire vessel, also in sensors-free zones. For the most critical situation (LVI test), a safety distance of 50 mm from the impact point to the closest fiber segment was deemed sufficient.

A pre-processing step for the iFEM model requires a filtering process of the strain extracted from the experimental network, to obtain clean strain values, minimizing the noise present. This was performed using a Butterworth filter, with a cutoff frequency of 0.1 Hz, as shown in Fig. 6 (c), where this filtering process was applied to a representative measurement point (sensor n°200 of Fig. 8(a)). In addition to this, the sensors were purified with outliers and the strains were processed by adapting the measurements to the mesh of the iFEM model that will be explained subsequently.

After filtering the experimental measurements, the strain pattern extracted at the middle time instant of the constant loading phase of the quasi-static test is presented in Fig. 8.

Regarding the impact test patterns, only the one corresponding to the moment of maximum impactor penetration, for simplicity, is shown in Fig. 9. Finally, the sampling frequency was 3.84 Hz for the quasi-static

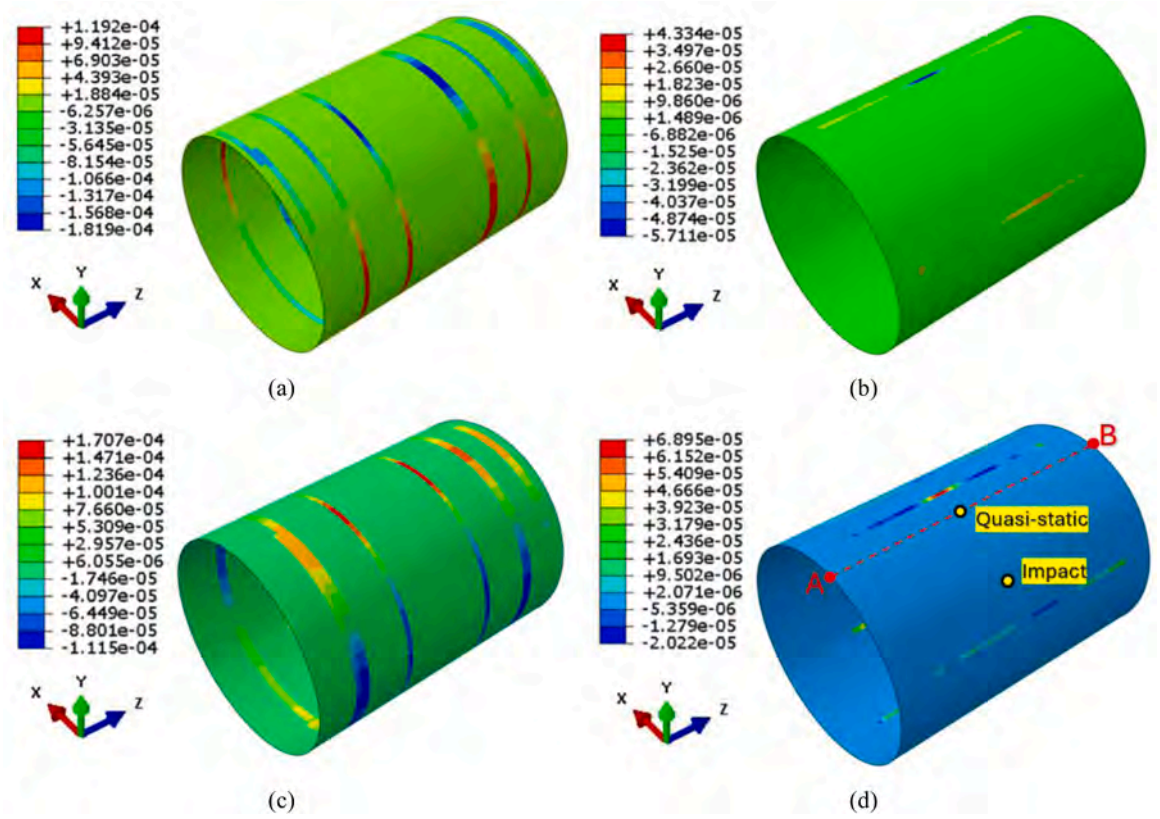

Fig. 11. Sensor network of strain gauges measurement extracted to the experimental sensor network for the quasi-static test (unit of measurement: [–]) plotted on the surface of the cylinder: (a) $\varepsilon_{circumferential}$ (external), (b) ε_{axial} (external), (c) $\varepsilon_{circumferential}$ (internal) and (d) ε_{axial} (internal).

case and 3 kHz for the impact scenario.

3.3. The iFEM model with strain pre-extrapolation

The iFEM model comprises 8160 iQS4 elements [26], with boundary conditions applied as hinges along the x-direction paths corresponding to the V-shaped support used in the experimental tests (Fig. 10). As mentioned in Section 2, no information regarding load or material properties is provided to the iFEM, allowing for complete displacement and strain field reconstructions.

In a previous study by the authors [666], the displacement and strain field reconstruction were performed using iFEM based solely on the experimental strain measurements, $\boldsymbol{\varepsilon}_{in}$, from the sensor network described above (quasi-static scenario, see Fig. 8). Compared to the previous work, this study involves a pre-extrapolation technique on the iSQ4 elements without any experimental strain values. This physics-based pre-extrapolation approach was explained in detail in Section 2.

The procedure was applied to the unwrapped cylinder, emulating a plate, while imposing equal values on the sides at the ends of the x-axis, thereby ensuring continuity along the circumference.

The application of the aforementioned physics-based strain pre-extrapolation procedure performed on the strain patterns of Fig. 8 is shown in Fig. 12, considering axial and circumferential strain component separated. Regarding the instant taken far from the LVI test, the pre-extrapolation procedure brought to the axial strain fields presented in Fig. 13.

Although the procedure was applied to all the strain patterns considered in this study, to avoid overloading the discussion, only the cases in Figs. 10 and 12 are shown.

3.4. Shape sensing and damage detection results

The results of the reconstruction provided by iFEM about the instant considered in the quasi-static compression test, are shown in Fig. 14, considering as strain $\boldsymbol{\varepsilon}_{in}$ the one of Fig. 12, where the weight of the matrix $\boldsymbol{W}$ for the mesh elements in the iFEM model without sensors is set to one, as this value yields the best results.

The results obtained, as far as the reconstruction of the vessel's displacement and strain field is concerned, are both qualitatively and quantitatively accurate and representative of the authors' expectations.

Because no direct experimental displacement measurements were taken during the test, a validation of the iFEM displacement was performed by comparing the vertical displacement (U2) derived from iFEM at the point of load application (yellow point in Fig. 14(c), $U_{iFEM} = 0.127\ mm$) with the testing machine cross-head displacement ($U_{Machine} = 0.198\ mm$), the latter compensated to consider the deformability of the testing machine not considered in the iFEM model.

Although the iFEM slightly underestimates the vertical displacement, this result is deemed reasonable. The discrepancy is likely due to unquantifiable factors, as the load application area exhibits highly nonlinear behavior and lacks sensors near capture this effect accurately, resulting in an underestimation of the displacement in the iFEM reconstruction for this region. While this issue is considered the primary source of the discrepancy, additional factors that may increase uncertainty include the following: slight misalignment between the inner and outer paths of the sensor network, minor irregularities in the vessel's lateral surface due to the inherent characteristics of the filament winding process, and micro-failures in constraints observed during the quasi-static compression test.

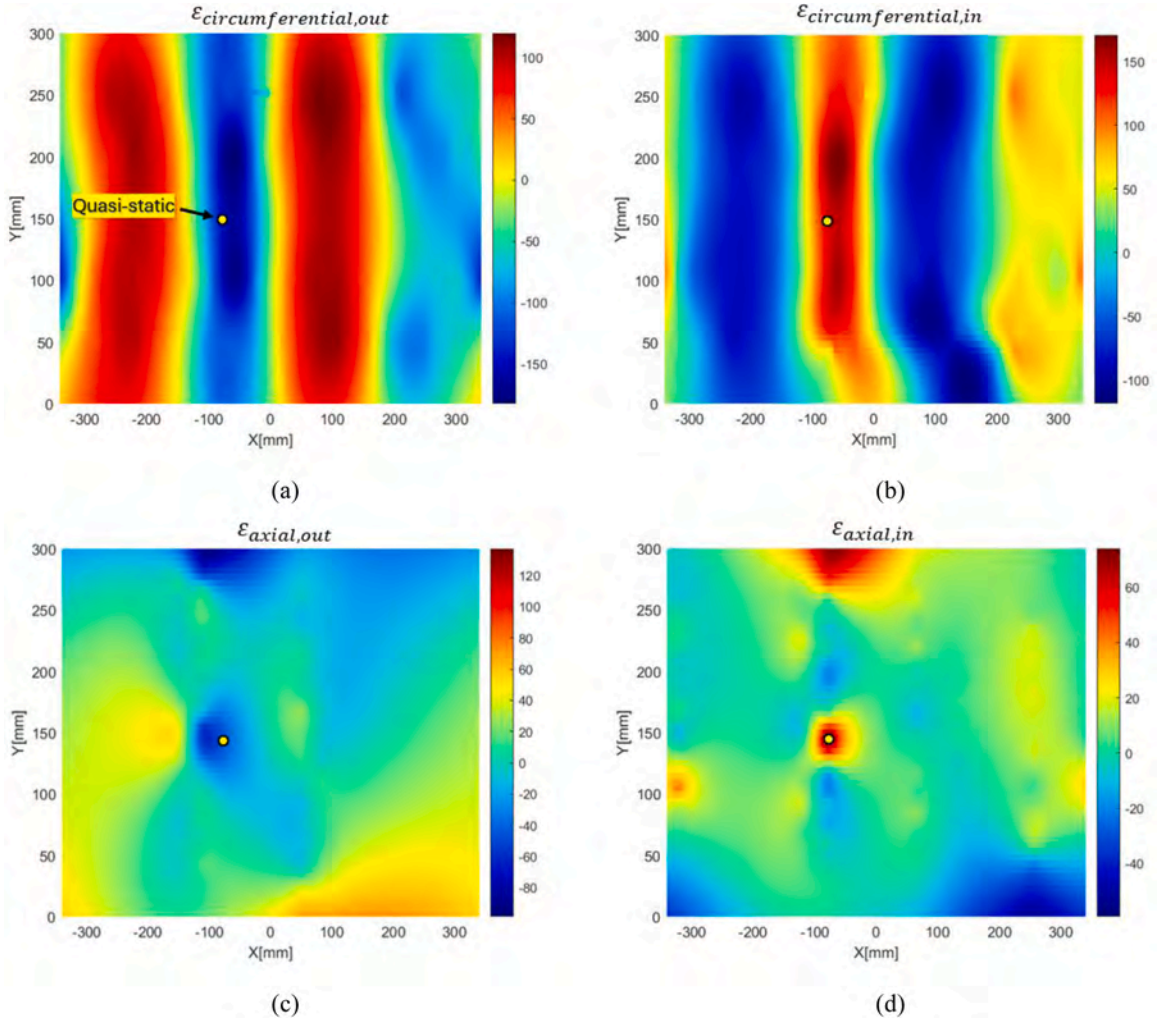

Fig. 12. Strain pattern considered as input $\boldsymbol{\varepsilon}_{in}$ when it comes to the quasi-static test considering physics-based pre-extrapolation (unit of measurement: [$\mu\varepsilon$]): (a) $\varepsilon_{circumferential}$ (external), (b) $\varepsilon_{circumferential}$ (internal), (c) ε_{axial} (external) and (d) ε_{axial} (internal).

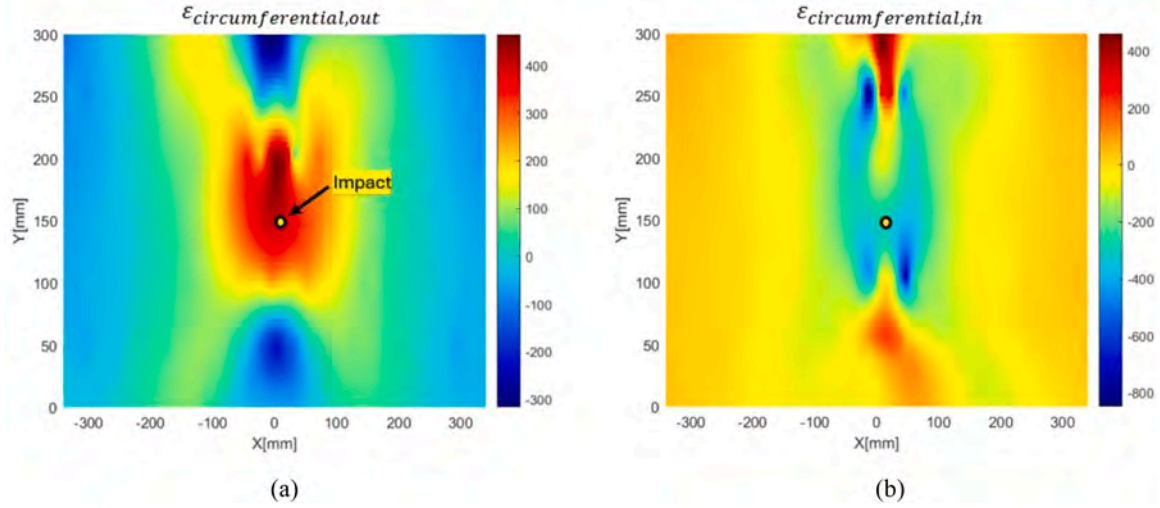

Fig. 13. Strain pattern considered as input $\boldsymbol{\varepsilon}_{in}$ when it comes to the instant far from the LVI test considering physics-based pre-extrapolation (unit of measurement: [$\mu\varepsilon$]): (a) $\varepsilon_{circumferential}$ (external) and (b) $\varepsilon_{circumferential}$ (internal).

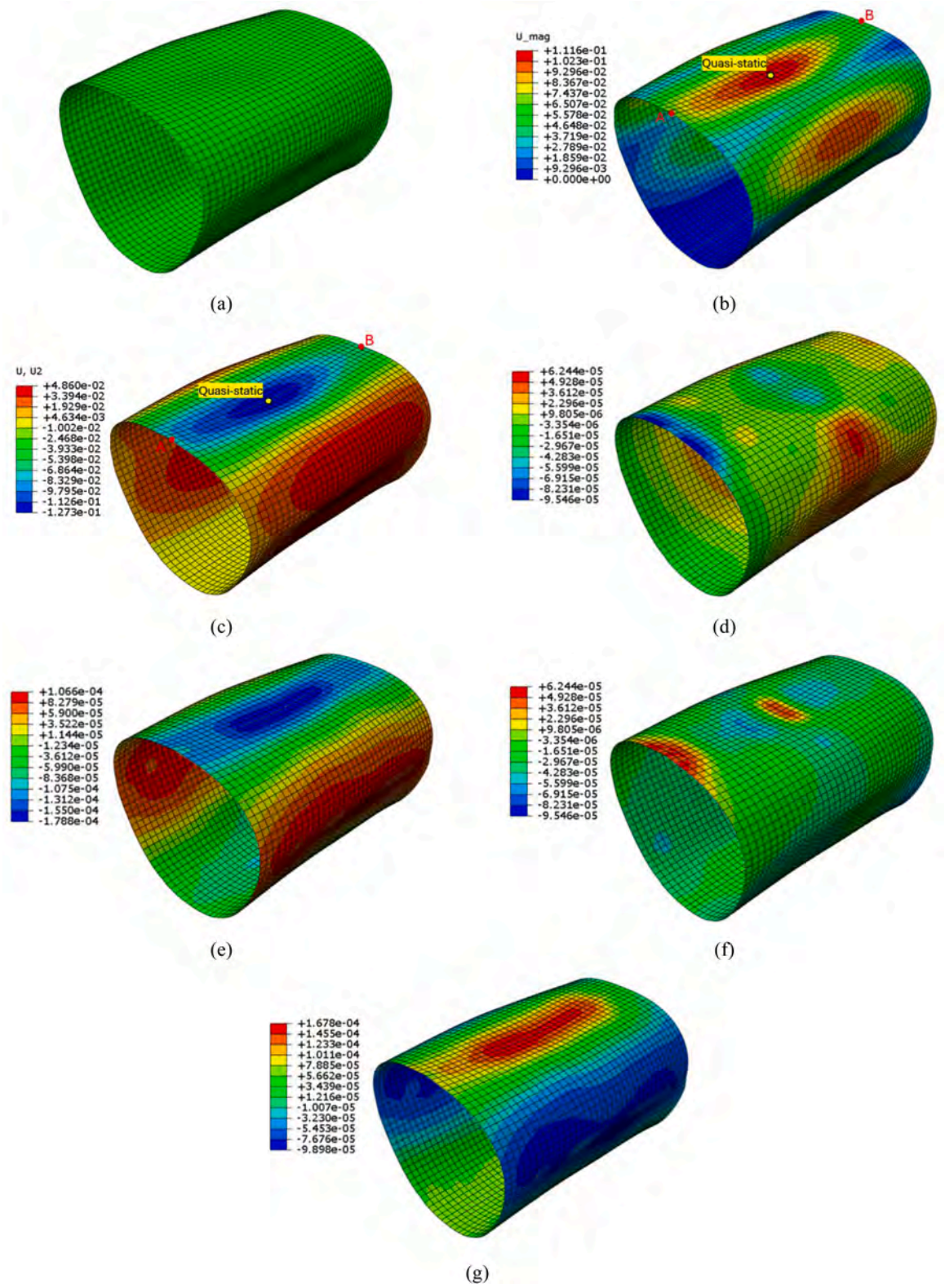

Fig. 14. Reconstruction results of the full field of displacements and strains (deformation scale factor = 600, displacement in [mm] and strain in [-]) for the quasi-static test at the middle instant of constant loading phase: (a) deformed configuration without any results, (b) total displacements U_mag, (c) vertical displacements U2, (d) $\varepsilon_{circumferential}$ (external), (e) ε_{axial} (external), (f) $\varepsilon_{circumferential}$ (internal) and (g) ε_{axial} (internal). same reference system of Fig. 11.

To perform a second check regarding the accuracy of the results obtained for the quasi-static case and the correctness of the weight value associated with the pre-extrapolated measurements, the authors carried out a verification of the strain reconstruction on an external lateral path of the cylinder, corresponding to a limited portion of the sensor network (axial piece of path of the sensor network, Fig. 15). In this case, the experimental measurements corresponding to the specific axial path highlighted in Fig. 15 are not provided as input to the iFEM; instead, the

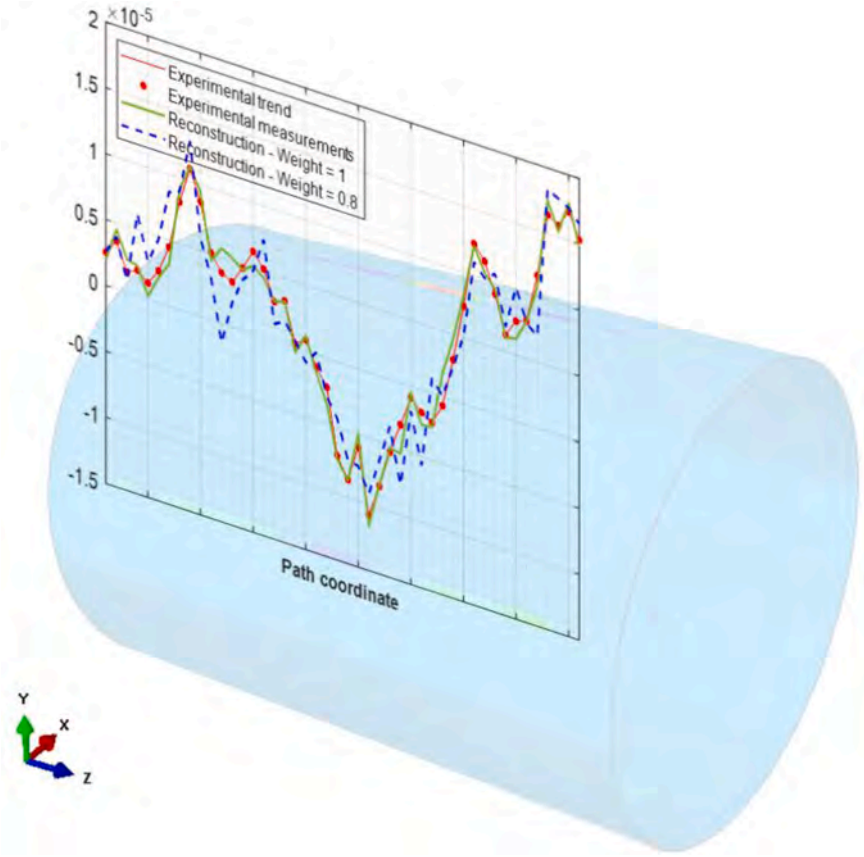

Fig. 15. Comparison between the strain reconstructed by iFEM (ε_{axial} external) and the experimental one, at some locations of a lateral segment belonging to the sensor network (unit of measurement: [-]), considering three different values of weight associated to the pre-extrapolated measurements.

proposed physics-based pre-extrapolation strategy is applied along this segment. All the measurements of this axial segment were used for a posteriori validation by comparing experimental strain data with those reconstructed by the iFEM, thereby demonstrating the reliability of the previous results. Different weight values associated with the pre-extrapolated measurements were tested; however, for simplicity, only the results corresponding to weights 0.8 and 1 are presented here.

As illustrated in Fig. 15, the weight coefficient that guarantees the best reconstruction of the strain pattern along the segment is equal to 1. This case indicates accurate strain reconstruction along the path and, consequently, a reliable displacement estimation. Considering weights progressively smaller than 1, the reconstruction quality deteriorates.

The verification just performed was extended to other segments of the sensor network, but the result remained the same, confirming that the optimal weight in this case is equal to 1. The latter cases are not reported here for brevity. The optimal (unitary) value assigned to the pre-extrapolated measurements highlights that physics-based strain extrapolation methodology is highly effective in compensating for the lack of sensors in certain areas of the structure, as it produces strains that are consistent with the underlying physics of the problem.

Overall, the results presented in Fig. 14 demonstrate that the iFEM, when combined with the pre-extrapolation strategy, was capable of accurately and satisfactorily reconstructing both the displacement and strain fields. This performance was specifically observed in the context of a quasi-static experimental case, highlighting the effectiveness of the proposed methodology in dealing with regions lacking physical sensors.

Regarding the LVI case, Fig. 16 presents the sequence of displacement field reconstructions provided by the iFEM for five time instants along the force vs displacement curve shown in Fig. 6(b). Each reconstruction represents the dynamic behavior of the system at specific points on the curve, offering a detailed view of the structural response and motion. The same figure also shows a comparison between the reconstructed vertical displacement at the point of contact with the impactor and the displacement measured by the machine's crosshead, for correlation and validation of the iFEM model used for reconstruction.

Although the reconstructed vertical displacement values show a slight discrepancy when compared to the experimental ones, the same unquantifiable factors described earlier must be considered to explain this difference. In addition to the factors already mentioned, it is important to note that the impact test generates a highly localized non-linear behavior in the load application zone, accompanied by visible plastic indentation that is easily observable (Fig. 17). These complex effects are not considered in the iFEM model used for the reconstruction, and as such, the authors believe that the results obtained for the LVI case remain highly reliable, despite the discrepancies observed in the displacement fields.

Similarly to the validation performed for the quasi-static test results, the effectiveness of the iFEM in reconstructing the strains along specific paths of the sensor network was verified, enabling a posteriori validation, exactly with the approach shown in Fig. 15. For simplicity, the results are not presented here; however, they once again confirm the reliability of the obtained outcomes. In this case as well, the optimal weight for the extrapolated regions of the iFEM model was set to one.

The final aspect addressed in this study concerns the reconstruction of the displacement and strain fields using iFEM, based on a strain pattern obtained sufficiently after the LVI test. In this case, the question is whether the resulting strain pattern shows signs of residual deformations after the impact, with the aim of performing damage detection and localization. The reconstructions mentioned above are shown in Fig. 18, with a scale factor of 1000 applied to the displacement contour.

Based on the results provided in Fig. 18, a permanent deformation

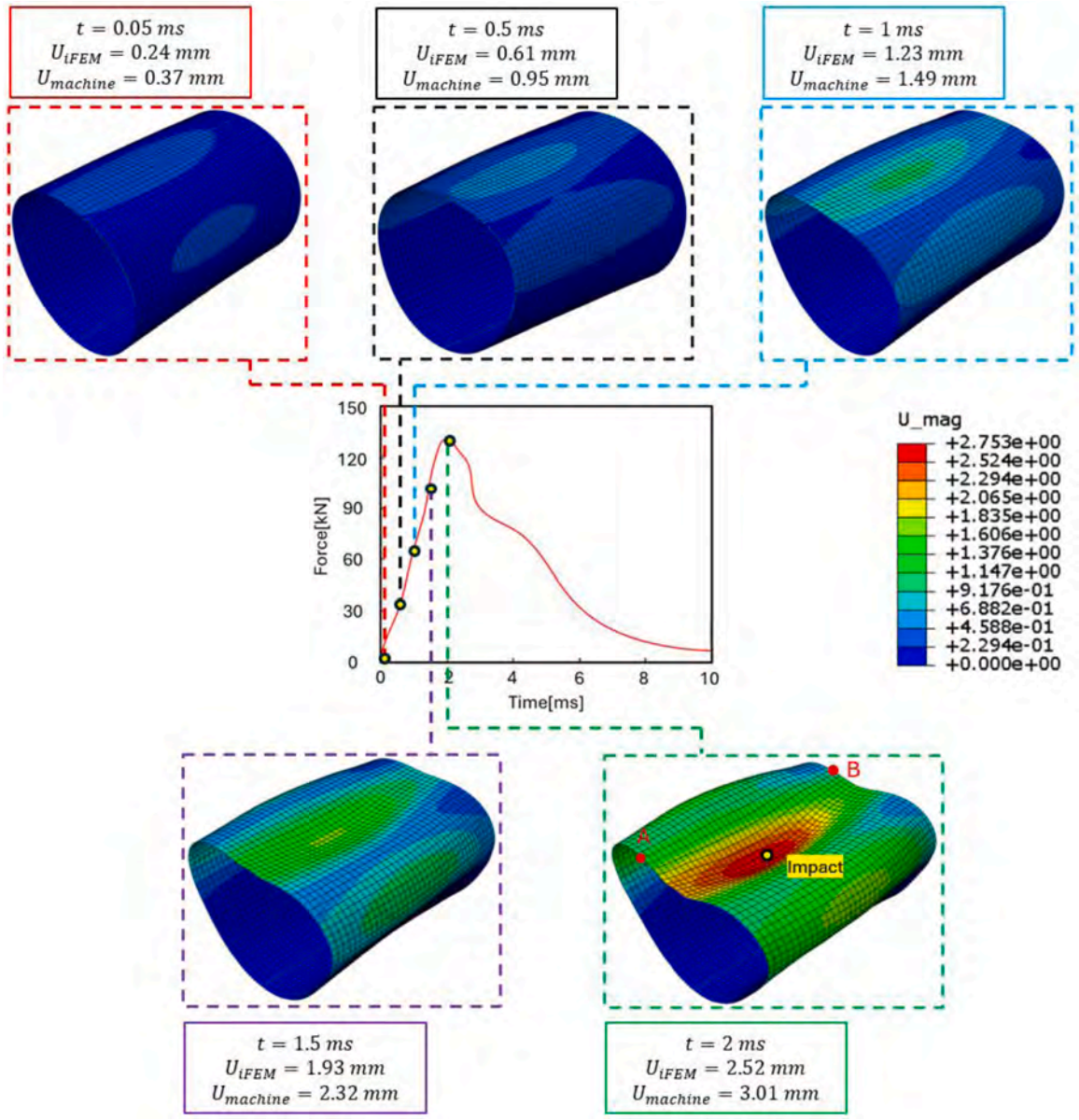

Fig. 16. Reconstruction results of the full field of displacements (total displacements U_mag, deformation scale factor = 30, all measures in mm) for several time instants of the low-velocity impact test. all contours have the same legend, identified on the right. same reference system of Fig. 11.

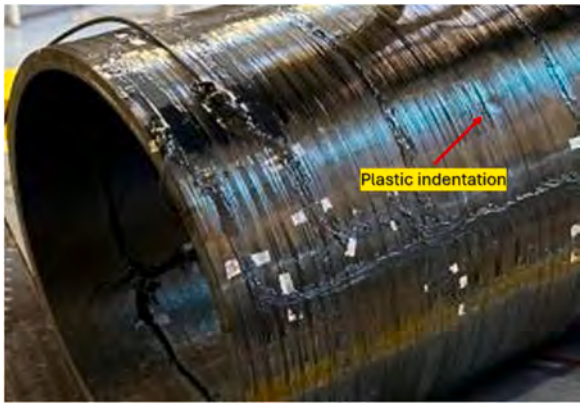

Fig. 17. Magnification of the local plastic indentation visible on the sample after the LVI test.

(and so residual strain) is clearly evident, although small, in the area where the impact occurred, from both displacement magnitude and ε_{axial} internal plot contours. The contours shown in Fig. 18(a) may lead to a counterintuitive deformation pattern in the outer layers of the filament-wound cylinder following impact. Despite the external-to-internal direction of the impact force, the post-impact deformation exhibits a positive strain (outward expansion) in the outer layers. This behavior can be attributed to the redistribution of residual stresses within the composite structure. Prior to impact, as highlighted by Ref [72], the outer layers experience compressive residual stresses due to the manufacturing process, while the inner layers are subjected to tensile residual stresses. The LVI test induces local delamination and damage, disrupting the interlaminar continuity. This disruption relaxes the compressive stresses in the outer layers, allowing them to expand outward, while the inner layers, relieved of tensile constraints, may undergo slight inward deformation. This redistribution highlights the critical role of residual stresses in governing the mechanical response of composite structures under dynamic loading.

Although the paper does not investigate this aspect in detail, the

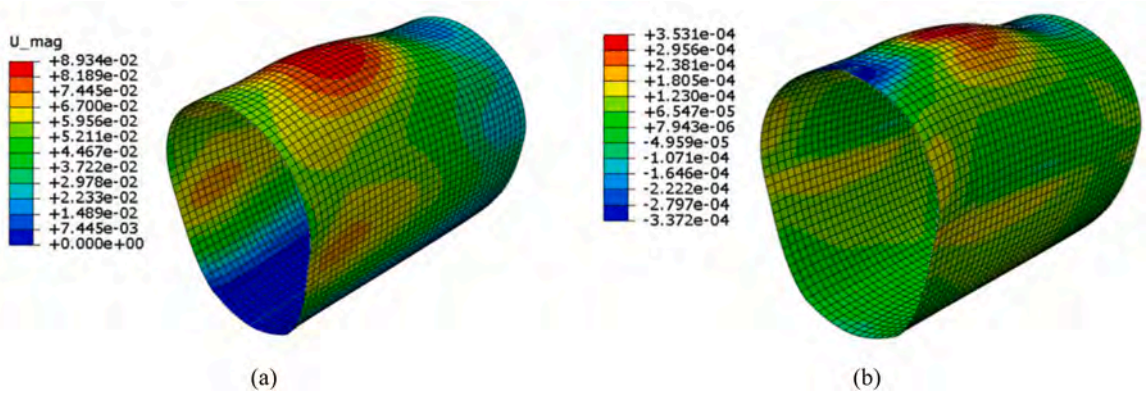

Fig. 18. Reconstruction results of the full field of displacements and strains (deformation scale factor = 1000, displacement in [mm] and strain in [-]) considering an instant sufficiently far from the LVI test: (a) total displacements U_mag and (b) $\varepsilon_{circumferential}$ (external). same reference system of Fig. 11.

authors have attempted to provide a potential explanation for this phenomenon. In any case, they are confident in asserting that the iFEM reconstruction was performed in alignment with the experimental data, yielding consistent and reliable results under this condition also.

Overall, the application of the iFEM strategy to the experimental case under investigation demonstrated exceptional effectiveness in shape sensing and damage detection across various loading conditions (quasi-static and dynamic). This confirms its reliability even under non-trivial loading scenarios for type-IV pressure vessels. The validation through experimental values further reinforces the accuracy and credibility of the reconstructed results presented.

4. Concluding remarks

In this study, the iFEM strategy was applied to a type IV pressure vessel prototype to evaluate its capability in reconstructing displacement and strain fields under complex loading conditions. Experimental strain data were collected using a sensor network composed of axial and circumferential segments during quasi-static compression and low-velocity impact tests on the lateral surface of the sample. To overcome the challenge of limited strain data availability across the entire vessel, a physics-based strain pre-extrapolation strategy was integrated into the framework, based on the governing equation of plate's bending theory. Furthermore, the effectiveness of the iFEM in detecting impact-induced damage was demonstrated through the analysis of residual strains recorded after the impact.

For the quasi-static compression test, the reconstruction was focused on the middle instant of the constant loading phase, where the maximum compression occurred. The reconstructed displacement field results, when compared to the values recorded by the testing machine, confirm an excellent match between the experimental and reconstructed data, even in cases where the compression point lies in a sensor-free zone. Additionally, the influence of the weighting factor assigned to the pre-extrapolated measurements was investigated, revealing that the optimal weight is unitary. This outcome is attributed to the fact that the chosen pre-extrapolation method ensures strain fields provided to the iFEM are highly consistent with the physics of the problem.

For the LVI case, the iFEM successfully reconstructed displacement fields at five key time instants, capturing the dynamic behavior of the structure. While some discrepancies were observed between the reconstructed and experimental vertical displacements at the impact point, these are attributed to localized non-linear effects and plastic indentation, which are not accounted for in the iFEM model. Despite this, the results remain highly reliable. The iFEM also proved effective in strain reconstruction along specific sensor paths, confirming the accuracy of the method, with an optimal weight of one for extrapolated regions, like in the quasi-static case.

Finally, the iFEM reconstruction, using a strain pattern extracted at a time sufficiently distant from the impact, unequivocally detects residual strains associated with impact damage, enabling effective damage detection and localization. Overall, the iFEM demonstrated the ability to accurately reconstruct both the displacement and strain fields under various complex loading conditions on the type IV pressure vessel prototype, showcasing exceptional capabilities in handling both static and dynamic cases, as well as situations where the strain field indicates the presence of damage.

Despite the promising results, some limitations of this study should be acknowledged. First, the iFEM formulation does not account for material nonlinearity or damage progression in the constitutive behavior, which may affect the accuracy of the displacement reconstruction under severe post-impact conditions. Additionally, although the fiber layout was carefully designed, the inner-to-outer correspondence is not perfect due to practical installation constraints. Another limitation concerns the mesh discretization: the need to assign one strain input per element centroid inherently filters part of the rich distributed data provided by the optical fiber, potentially neglecting high-frequency strain gradients. Finally, the damage detection was based solely on residual strain interpretation, and future work will aim at validating this aspect through complementary diagnostic methods such as ultrasound or CT scans.

CRediT authorship contribution statement

Jacopo Bardiani: Writing – review & editing, Writing – original draft, Visualization, Validation, Methodology, Investigation, Formal analysis, Data curation, Conceptualization. **Roberto Faure Ragani:** Writing – review & editing, Writing – original draft, Visualization, Validation, Methodology, Investigation, Formal analysis, Data curation, Conceptualization. **Lucio Pinello:** Investigation, Formal analysis, Data curation. **Adnan Kefal:** Writing – review & editing, Methodology, Conceptualization. **Andrea Manes:** Writing – review & editing, Supervision, Resources, Project administration, Methodology. **Claudio Sbarufatti:** Writing – review & editing, Supervision, Resources, Project administration, Methodology, Conceptualization.

Declaration of competing interest

The authors declare that they have no known competing financial interests or personal relationships that could have appeared to influence the work reported in this paper.

Acknowledgements

The author(s) thank Faber Industrie SpA for their support in providing the pressure vessel samples used in the experimental tests and for offering their expertise and guidance, which were invaluable in

achieving the objectives of this manuscript.

Data availability

The data given in this article are the data supporting the results of this study are available upon request.

References

[1] R. Sharma, A. Pachauri, A Review of Pressure Vessels Regarding Their Design, Manufacturing, Testing, Materials, and Inspection, Mater Today Proc, 2023, https://doi.org/10.1016/j.matpr.2023.03.258.

[2] M.A. Rosen, S. Koohi-Fayegh, The prospects for hydrogen as an energy carrier: an overview of hydrogen energy and hydrogen energy systems, Energy Ecol. Environ., 1 (2016) 10–29.

[3] P.F. Liu, J.K. Chu, S.J. Hou, P. Xu, J.Y. Zheng, Numerical simulation and optimal design for composite high-pressure hydrogen storage vessel: a review, Renew. Sustain. Energy Rev. 16 (4) (2012) 1817–1827.

[4] D. Melideo, U. Desideri, The use of hydrogen as alternative fuel for ship propulsion: a case study of full and partial retrofitting of roll-on/roll-off vessels for short distance routes, Int. J. Hydrog. Energy 50 (2024) 1045–1055, https://doi.org/10.1016/j.ijhydene.2023.10.142.

[5] J.P.B. Ramirez, D. Halm, J.C. Grandidier, S. Villalonga, F. Nony, 700 bar type IV high pressure hydrogen storage vessel burst–simulation and experimental validation, Int. J. Hydrog. Energy 40 (38) (2015) 13183–13192.

[6] R. Santos, D. Vandepitte, D. Moens, Prediction of composite pressure vessels' burst strength through machine learning, Compos. Struct. 351 (2025) 118617.

[7] A. Kumar, R. Tripathi, Safety challenges and future scope of green hydrogen for the energy transition, Hydrog. Energy (2024) 303–324.

[8] J.A. Okolie, B.R. Patra, A. Mukherjee, S. Nanda, A.K. Dalai, J.A. Kozinski, Futuristic applications of hydrogen in energy, biorefining, aerospace, pharmaceuticals and metallurgy, Int. J. Hydrog. Energy 46 (13) (2021) 8885–8905.

[9] M.M. Prabhakar, N. Rajini, N. Ayrilmis, K. Mayandi, S. Siengchin, K. Senthilkumar, S. Karthikeyan, S.O. Ismail, An overview of burst, buckling, durability and corrosion analysis of lightweight FRP composite pipes and their applicability, Compos. Struct. 230 (2019) 111419.

[10] M. Nebe, T.J. Asijee, C. Braun, J.M.J.F. Van Campen, F. Walther, Experimental and analytical analysis on the stacking sequence of composite pressure vessels, Compos. Struct. 247 (2020) 112429.

[11] H. Barthelemy, M. Weber, F. Barbier, Hydrogen storage: recent improvements and industrial perspectives, Int. J. Hydrog. Energy 42 (2017) 7254–7262, https://doi.org/10.1016/j.ijhydene.2016.03.178.

[12] M. Ueda, T. Hidaka, N. Ichihara, H. Yang, W. Iwase, T. Matsuda, N. Morita, R. Aoki, T. Yokozeki, Voids in type-IV composite pressure vessels manufactured by a dry filament-winding process, Int. J. Press. Vessel. Pip. 208 (2024) 105154.

[13] E. Lainé, J.C. Dupré, J.C. Grandidier, M. Cruz, Instrumented tests on composite pressure vessels (type IV) under internal water pressure, Int. J. Hydrog. Energy 46 (2021) 1334–1346, https://doi.org/10.1016/j.ijhydene.2020.09.160.

[14] R.A. Weerts, O. Cousigne, K. Kunze, M.G. Geers, J.J. Remmers, Assessment of contact-induced damage mechanisms in thick-walled composite cylinders, J. Reinf. Plast. Compos. 39 (17–18) (2020) 679–699.

[15] M. Nebe, A. Johman, C. Braun, J.M.J.F. Van Campen, The effect of stacking sequence and circumferential ply drop locations on the mechanical response of type IV composite pressure vessels subjected to internal pressure: a numerical and experimental study, Compos. Struct. 294 (2022) 115585.

[16] J.S. Park, C.S. Hong, C.G. Kim, C.U. Kim, Analysis of filament wound composite structures considering the change of winding angles through the thickness direction, Compos. Struct. 55 (1) (2002) 63–71.

[17] M. Nachtane, M. Tarfaoui, M.A. Abichou, A. Vetcher, M. Rouway, A. Aâmir, H. Mouadili, H. Laaouidi, H. Naanani, An overview of the recent advances in composite materials and artificial intelligence for hydrogen storage vessels design, J. Compos. Sci. (2023), https://doi.org/10.3390/jcs7030119.

[18] A. Silva-Campillo, F. Pérez-Arribas, J.C. Suárez-Bermejo, Health-monitoring systems for marine structures: a review, Sensors (2023), https://doi.org/10.3390/s23042099.

[19] J. Bardiani, C. Oppezzo, A. Manes, C. Sbarufatti, An inverse FEM for structural health monitoring of a containership: sensor network optimization for accurate displacement, strain, and internal force reconstruction, Sensors 25 (1) (2025) 276, https://doi.org/10.3390/s25010276.

[20] A. Deraemaeker, E. Reynders, G. De Roeck, J. Kullaa, Vibration-based structural health monitoring using output-only measurements under changing environment, Mech. Syst. Signal Process. 22 (2008) 34–56, https://doi.org/10.1016/j.ymssp.2007.07.004.

[21] J.E. Warner, G.F. Bomarito, J.D. Hochhalter, W.P. Leser, P.E. Leser, J.A. Newman, A computationally-efficient probabilistic approach to model-based damage diagnosis, Int J. Progn. Manag. 8 (2) (2017), 026.

[22] M. Gherlone, P. Cerracchio, M. Mattone, Shape sensing methods: review and experimental comparison on a wing-shaped plate, Prog. Aerosp. Sci. 99 (2018) 14–26.

[23] Tessler, A., Spangler, J.L., 2003. A variational principle for reconstruction of elastic deformations in shear deformable plates and shells.

[24] A. Tessler, J.L. Spangler, A least-squares variational method for full-field reconstruction of elastic deformations in shear-deformable plates and shells, Comput. Methods Appl. Mech. Eng. 194 (2005) 327–339, https://doi.org/10.1016/j.cma.2004.03.015.

[25] A. Tessler, J.L. Spangler, Inverse FEM For Full-Field Reconstruction of Elastic Deformations in Shear Deformable Plates and Shells, January, 2nd European Workshop on Structural Health Monitoring, 2004.

[26] A. Kefal, E. Oterkus, A. Tessler, J.L. Spangler, A quadrilateral inverse-shell element with drilling degrees of freedom for shape sensing and structural health monitoring. engineering science and technology, an, Int. J. 19 (2016) 1299–1313, https://doi.org/10.1016/j.jestch.2016.03.006.

[27] A. Kefal, An efficient curved inverse-shell element for shape sensing and structural health monitoring of cylindrical marine structures, Ocean Eng. 188 (2019) 106262.

[28] A. Kefal, E. Oterkus, Displacement and stress monitoring of a Panamax containership using inverse finite element method, Ocean Eng. 119 (2016) 16–29, https://doi.org/10.1016/j.oceaneng.2016.04.025.

[29] J. Bardiani, A. Manes, M. Giglio, C. Sbarufatti, Shape sensing and damage identification with iFEM on a double bottom structure of a containership, eds, in: F. Concli, L. Maccioni, R. Vidoni, D.T. Matt (Eds.), Latest Advancements in Mechanical Engineering. ISIEA 2024, Latest Advancements in Mechanical Engineering. ISIEA 2024, 1124, Lecture Notes in Networks and Systems, Cham, 2024, https://doi.org/10.1007/978-3-031-70462-8_22. Springer.

[30] A. Kefal, J.B. Mayang, E. Oterkus, M. Yildiz, Three dimensional shape and stress monitoring of bulk carriers based on iFEM methodology, Ocean Eng. 147 (2018) 256–267, https://doi.org/10.1016/j.oceaneng.2017.10.040.

[31] A. Kefal, E. Oterkus, Displacement and stress monitoring of a chemical tanker based on inverse finite element method, Ocean Eng. 112 (2016) 33–46.

[32] M. Li, A. Kefal, E. Oterkus, S. Oterkus, Structural health monitoring of an offshore wind turbine tower using iFEM methodology, Ocean Eng. 204 (2020) 107291.

[33] D. Oboe, L. Colombo, C. Sbarufatti, M. Giglio, Shape sensing of a complex aeronautical structure with inverse finite element method, Sensors 21 (4) (2021) 1388.

[34] M. Esposito, M. Gherlone, Composite wing box deformed-shape reconstruction based on measured strains: optimization and comparison of existing approaches, Aerosp. Sci. Technol. 99 (2020) 105758.

[35] M. Esposito, M. Gherlone, P. Marzocca, External loads identification and shape sensing on an aluminum wing box: an integrated approach, Aerosp. Sci. Technol. 114 (2021) 106743.

[36] M.A. Abdollahzadeh, M.Y. Belur, M.F. Basoglu, A. Kefal, Shape Sensing of Beam-Like Structures Using the Robust iFEM-iQS4 Inverse Shell Element, IEEE Transactions on Instrumentation and Measurement, 2023.

[37] L. Colombo, C. Sbarufatti, M. Giglio, Definition of a load adaptive baseline by inverse finite element method for structural damage identification, Mech. Syst. Signal Process. 120 (2019) 584–607.

[38] M.A. Abdollahzadeh, A. Kefal, M. Yildiz, A comparative and review study on shape and stress sensing of flat/curved shell geometries using C0-continuous family of iFEM elements, Sensors 20 (14) (2020) 3808.

[39] M. Li, A. Kefal, B.C. Cerik, E. Oterkus, Dent damage identification in stiffened cylindrical structures using inverse Finite element method, Ocean Eng. 198 (2020), https://doi.org/10.1016/j.oceaneng.2020.106944.

[40] M. Ghasemzadeh, M. Mokhtari, M.H. Bilgin, A. Kefal, Pitting corrosion identification approach based on inverse finite element method for marine structure applications, Ocean Eng. 273 (2023) 113953.

[41] M. Esposito, M. Mattone, M. Gherlone, Experimental shape sensing and load identification on a stiffened panel: a comparative study, Sensors 22 (3) (2022) 1064.

[42] M.Y. Belur, A. Kefal, M.A. Abdollahzadeh, S.D. Fassois, Damage diagnosis of plates and shells through modal parameters reconstruction using inverse finite-element method, Struct. Health Monit. (2024), 14759217241249678.

[43] M. Gherlone, P. Cerracchio, M. Mattone, M. Di Sciuva, A. Tessler, Shape sensing of 3D frame structures using an inverse finite element method, Int. J. Solids Struct. 49 (22) (2012) 3100–3112.

[44] M. Gherlone, P. Cerracchio, M. Mattone, M. Di Sciuva, A. Tessler, An inverse finite element method for beam shape sensing: theoretical framework and experimental validation, Smart Mater. Struct. 23 (4) (2014) 045027.

[45] R. You, L. Ren, An enhanced inverse beam element for shape estimation of beam-like structures, Measurement 181 (2021) 109575.

[46] M. Nedelcu, Optimisation of inverse Finite element method for shape sensing of thin-walled cylinders by using Generalised Beam Theory, Thin Walled Struct. 188 (2023) 110865, https://doi.org/10.1016/j.tws.2023.110865.

[47] I.D. Craiu, M. Nedelcu, Combining iFEM and GBT for accurate shape sensing and damage detection in truncated conical shells with circular cross-section, Ocean Eng. 311 (2024) 118811, https://doi.org/10.1016/j.oceaneng.2024.118811.

[48] F. Zhao, L. Xu, H. Bao, J. Du, Shape sensing of variable cross-section beam using the inverse finite element method and isogeometric analysis, Measurement 158 (2020) 107656.

[49] R. You, L. Ren, C. Yuan, G. Song, Two-dimensional deformation estimation of beam-like structures using inverse finite-element method: theoretical study and experimental validation, J. Eng. Mech. 147 (5) (2021) 04021019.

[50] F. Zhao, A. Kefal, H. Bao, Nonlinear deformation monitoring of elastic beams based on isogeometric iFEM approach, Int. J. Non Linear Mech. 147 (2022) 104229.

[51] P. Cerracchio, M. Gherlone, M. Di Sciuva, A. Tessler, A novel approach for displacement and stress monitoring of sandwich structures based on the inverse Finite element method, Compos. Struct. 127 (2015) 69–76.

[52] A. Kefal, A. Tessler, E. Oterkus, An enhanced inverse finite element method for displacement and stress monitoring of multilayered composite and sandwich structures, Compos. Struct. 179 (2017) 514–540.

[53] F. Zhao, H. Bao, J. Liu, K. Li, Shape sensing of multilayered composite and sandwich beams based on Refined Zigzag theory and inverse finite element method, Compos. Struct. 261 (2021) 113321.
[54] A. Kefal, I.E. Tabrizi, M. Tansan, E. Kisa, M. Yildiz, An experimental implementation of inverse finite element method for real-time shape and strain sensing of composite and sandwich structures, Compos. Struct. 258 (2021) 113431.
[55] L. Colombo, D. Oboe, C. Sbarufatti, F. Cadini, S. Russo, M. Giglio, Shape sensing and damage identification with iFEM on a composite structure subjected to impact damage and non-trivial boundary conditions, Mech. Syst. Signal Process. 148 (2021) 107163.
[56] F. Ganjdoust, A. Kefal, A. Tessler, A novel delamination damage detection strategy based on inverse finite element method for structural health monitoring of composite structures, Mech. Syst. Signal Process. 192 (2023) 110202.
[57] R. Roy, M. Gherlone, Delamination and skin-spar debond detection in composite structures using the inverse finite element method, Materials 16 (5) (2023) 1969.
[58] A. Kefal, C. Diyaroglu, M. Yildiz, E. Oterkus, Coupling of peridynamics and inverse finite element method for shape sensing and crack propagation monitoring of plate structures, Comput. Methods Appl. Mech. Eng. 391 (2022) 114520.
[59] D. Oboe, D. Poloni, C. Sbarufatti, M. Giglio, Towards automatic crack size estimation with iFEM for structural health monitoring, Sensors 23 (7) (2023) 3406.
[60] A. Kefal, E. Oterkus, Isogeometric iFEM analysis of thin shell structures, Sensors 20 (9) (2020) 2685.
[61] A. Kefal, I.E. Tabrizi, M. Yildiz, A. Tessler, A smoothed iFEM approach for efficient shape-sensing applications: numerical and experimental validation on composite structures, Mech. Syst. Signal Process. 152 (2021) 107486, https://doi.org/10.1016/j.ymssp.2020.107486.
[62] D. Oboe, L. Colombo, C. Sbarufatti, M. Giglio, Comparison of strain pre-extrapolation techniques for shape and strain sensing by iFEM of a composite plate subjected to compression buckling, Compos. Struct. 262 (2021) 113587.
[63] D. Oboe, C. Sbarufatti, M. Giglio, Physics-based strain pre-extrapolation technique for inverse Finite element method, Mech. Syst. Signal Process. 177 (2022), https://doi.org/10.1016/j.ymssp.2022.109167.
[64] D. Poloni, D. Oboe, C. Sbarufatti, M. Giglio, Towards a stochastic inverse Finite element method: a gaussian process strain extrapolation, Mech. Syst. Signal Process. 189 (2023), https://doi.org/10.1016/j.ymssp.2022.110056.
[65] D. Poloni, D. Oboe, C. Sbarufatti, M. Giglio, Variable thickness strain pre-extrapolation for the inverse finite element method, Sensors 23 (2023), https://doi.org/10.3390/s23031733.
[66] J. Bardiani, M. Giglio, A. Manes, C. Sbarufatti, Shape sensing with iFEM on a type IV pressure vessel based on experimental measurements, in: Proceedings of the 10th European Workshop on Structural Health Monitoring (EWSHM 2024) 29, 2024, https://doi.org/10.58286/29654. June 10-13, 2024 in Potsdam, Germany. e-Journal of nondestructive testing vol.
[67] J.N. Reddy, Theory and Analysis of Elastic Plates and Shells, CRC Press, 2006.
[68] A.P.S. Selvadurai, The Biharmonic equation, in: Partial Differential Equations in Mechanics 2: The Biharmonic Equation, Poisson's Equation, Springer Berlin Heidelberg, Berlin, Heidelberg, 2000, https://doi.org/10.1007/978-3-662-09205-7_1, 1–502.
[69] Gazzola, F., Grunau, H.C., Sweers, G., 2010. Polyharmonic boundary value problems.
[70] R.A.J. Weerts, O. Cousigné, K. Kunze, M.G.D. Geers, J.J.C. Remmers, Assessment of contact-induced damage mechanisms in thick-walled composite cylinders, J. Reinf. Plast. Compos. 39 (2020) 679–699, https://doi.org/10.1177/0731684420923043.
[71] D. Ma, M. Rezasefat, J. Aparecido da Cruz, S. Campos Amico, M. Giglio, A. Manes, Effect of fixture boundary conditions for low-velocity impact: a focus on composites with different matrix and fibers, Mater Lett. 355 (2024), https://doi.org/10.1016/j.matlet.2023.135370.
[72] Kang, C., Shi, Y., Deng, B., Yu, T., Sun, P., 2018. Determination of residual stress and design of process parameters for composite cylinder in filament winding. Advances in materials science and engineering 2018. https://doi.org/10.1155/2018/1821342.